

## BAR-INDUCED CENTRAL STAR FORMATION AS REVEALED BY INTEGRAL FIELD SPECTROSCOPY FROM CALIFA

LIN LIN<sup>1</sup>, CHENG LI<sup>2,1</sup>, YANQIN HE<sup>1,3</sup>, TING XIAO<sup>1</sup>, ENCI WANG<sup>1</sup>*Draft version October 8, 2021*

## ABSTRACT

We investigate the recent star formation history (SFH) in the inner region of 57 nearly face-on spiral galaxies selected from the Calar Alto Legacy Integral Field Area (CALIFA) survey. For each galaxy we use the integral field spectroscopy from CALIFA to obtain two-dimensional maps and radial profiles of three parameters that are sensitive indicators of the recent SFH: the 4000Å break ( $D_n(4000)$ ), and the equivalent width of H $\delta$  absorption ( $EW(H\delta_A)$ ) and H $\alpha$  emission ( $EW(H\alpha)$ ). We have also performed photometric decomposition of bulge/bar/disk components based on SDSS optical image. We identify a class of 17 “turnover” galaxies whose central region present significant drop in  $D_n(4000)$ , and most of them correspondingly show a central upturn in  $EW(H\delta_A)$  and  $EW(H\alpha)$ . This indicates that the central region of the turnover galaxies has experienced star formation in the past 1-2 Gyr, which makes the bulge younger and more star-forming than surrounding regions. We find almost all (15/17) the turnover galaxies are barred, while only half of the barred galaxies in our sample (15/32) are classified as a turnover galaxy. This finding provides strong evidence in support of the theoretical expectation that the bar may drive gas from the disc inward to trigger star formation in galaxy center, an important channel for the growth/rejuvenation of pseudobulges in disc galaxies.

*Subject headings:* galaxies: spiral - galaxies: structure - galaxies: formation - galaxies: evolution - galaxies: stellar content

## 1. INTRODUCTION

Bars are commonly found in spiral galaxies. In the local universe, about 30% disc galaxies are barred, and the fraction increases to 50-70% if weak bars are included or if NIR images are used for bar identification (e.g. de Vaucouleurs 1963; Knapen et al. 2000; Marinova & Jogee 2007; Eskridge et al. 2000; Masters et al. 2011; Lee et al. 2012). The bar fraction decreases with increasing redshift, dropping to about 20% for all bars and below 10% for strong bars at  $z \sim 0.8$  (Sheth et al. 2008). In theory and  $N$ -body simulations bars play crucial roles in driving the secular evolution of disc galaxies. Bars grow through transferring angular momentum to the outer disk, or even to the spheroid/halo (Athanasoula 2003). This process drives the gas in the disc either outward to form ring-like structure in the outskirts, or inward to trigger star formation in the central region (e.g. Athanasoula 1992; Sellwood & Wilkinson 1993; Piner et al. 1995; Knapen et al. 2000; Sheth et al. 2002; Regan & Teuben 2004; Zurita & Pérez 2008). The gas inflow to the center is believed to make pseudobulges (Kormendy & Kennicutt 2004, and reference therein).

Bar-induced gas inflow and the related central star formation have been reported in many observational studies. Compared with unbarred galaxies, barred galaxies are found to have higher gas concentrations (Sakamoto et al. 1999; Jogee et al. 2005; Sheth et al. 2005; Regan et al. 2006), higher cen-

tral star formation rates (SFRs) (de Jong et al. 1984; Hawarden et al. 1986; Devereux 1987; Puxley et al. 1988; Ho et al. 1997). Flatter chemical abundance gradients were found in barred galaxies from previous studies (Zaritsky et al. 1994; Martin & Roy 1994), while recent results shown no difference in gas-phase (Sánchez et al. 2014; Sánchez-Menguiano et al. 2016) or stellar (Cacho et al. 2014; Sánchez-Blázquez et al. 2014) metallicity gradients between galaxies with or without bar. A recent study by Wang et al. (2012) based on a volume-limited sample of galaxies in the Sloan Digital Sky Survey (SDSS; York et al. 2000) found strong correlation between the central-to-global SFR and the presence of a bar in face-on spiral galaxies: more than half of the galaxies with highly concentrated SFR are barred. The authors suggested that the central star formation of the other half galaxies which are unbarred may be triggered by tidal interactions with companion galaxies, an idea which is supported by the following two observational facts. On one hand, galaxy-galaxy interactions are known to be able to trigger strong star formation in galaxy centers (e.g. Li et al. 2008). On the other hand, the presence of a bar in galaxies is found to have weak/no correlation with galaxy-galaxy interactions (Li et al. 2009; Lin et al. 2014). These two findings combine to suggest that, the central star formation triggered by interactions and the central star formation induced by bar-driven gas inflow are distinct events, and both are expected to contribute to bulge growth.

Some studies suggested that bulges may be rejuvenated systems (Thomas & Davies 2006; Carollo et al. 2007; Obreja et al. 2013; Erwin et al. 2015). Old and young stellar populations coexist in one bulge and these two populations are kinematically distinguishable, with the old population having spheroid

<sup>1</sup> Shanghai Astronomical Observatory, Chinese Academy of Sciences, Shanghai 200030, China; linlin@shao.ac.cn

<sup>2</sup> Physics Department & Tsinghua Center for Astrophysics, Tsinghua University, Beijing 100084, China; cli2015@tsinghua.edu.cn

<sup>3</sup> Tianjin Astrophysics Center, Tianjin Normal University, Tianjin 300387, China

kinematics and the secondary population being rotationally supported (Emsellem et al. 2001; Pérez et al. 2009). High frequency of young stellar populations in bulges have been found in both barred galaxies (Coelho & Gadotti 2011; Méndez-Abreu et al. 2014) and close pairs (Kannappan et al. 2004), supporting both bars and interactions to be responsible for the rejuvenation of the central bulge.

Our understanding of the stellar populations and star formation history of different structural components in galaxies has improved rapidly in recent years, thanks to the many integral field spectroscopy (IFS) surveys. These surveys have obtained spatially resolved spectroscopy for samples of galaxies in the local Universe, providing both two-dimensional maps and radial profiles of the stellar population properties and kinematics across each galaxy. For instance, using data from the Calar Alto Legacy Integral Field Area (CALIFA) survey (Sánchez et al. 2012, 2016), Holmes et al. (2015) detected non-circular flows in 12 gas rich disc galaxies with intermediate inclinations, and found 11 of them have a bar, providing strong evidence in support of bars as the driver of gas flow and thus secular galaxy evolution. Another nice example of IFS observations of barred galaxies is presented in Gadotti et al. (2015) which studied kinematics and stellar population content of NGC 4371, a massive barred galaxy in the core of the Virgo Cluster, using data from the Multi-Unit Spectroscopic Explorer (MUSE), an IFS instrument recently commissioned at the VLT. The MUSE data revealed an inner disc and a nuclear ring, which are rotationally supported and dominated by stars older than 10 Gyr. This suggested the bar in the galaxy formed at  $z \sim 1.8$ , and thus may have an extended impact on the galaxy evolution over a long time.

In this work we make use of data from the second data release of the CALIFA survey (García-Benito et al. 2015) and study the recent star formation history of the inner region for 57 nearly face-on spiral galaxies. In particular, we aim to improve our understanding of the physical link between the central star formation history and the presence of the bar structure. For this purpose we measure three spectral indices:  $D_n(4000)$  (the break at around 4000 Å in optical spectra of galaxies),  $EW(H\delta_A)$  (equivalent width of the  $H\delta$  absorption line) and  $EW(H\alpha)$  (equivalent width of the  $H\alpha$  emission line), which are known to be sensitive indicators of stellar populations formed at different times in the past 1-2 Gyr. Therefore one may have an indication of the recent star formation history by combining the three parameters (e.g. Bruzual & Charlot 2003; Kauffmann et al. 2003; Li et al. 2015). As we will show, quite a large fraction of our galaxies show clear signature of recent/ongoing star formation in the central region and almost all these galaxies are barred. On the other hand, interestingly, the bar structure is presented in only half of the galaxies that show the central star formation.

We will first describe the CALIFA sample and our methodology of measuring the SFH diagnostic parameters (§2), and then present our results in §3. We discuss the implications of our results on bar-driven gas inflow and bulge growth/rejuvenation in §4, and summarize our conclusions in §5.

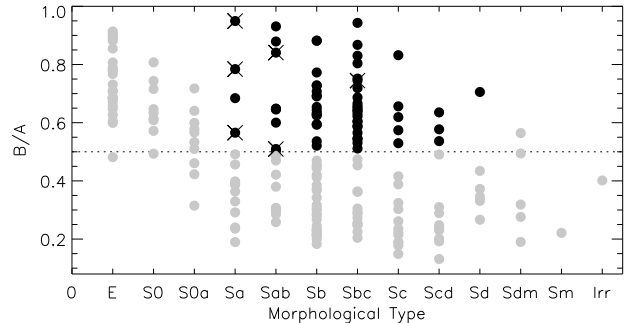


FIG. 1.— Distribution of morphological type and minor-to-major axis ratio ( $b/a$ ) for the CALIFA DR2 sample. The dashed line represents  $b/a=0.5$ , the divider we adopt to select face-on galaxies. The 57 face-on spiral galaxies studied in this paper are highlighted as solid black dots. The crosses indicate the galaxies with obvious dust-lane or merging systems, and these are excluded from our analysis.

## 2. DATA

### 2.1. The CALIFA survey

We use data from the second data release (DR2; García-Benito et al. (2015)) of the Calar Alto Legacy Integral Field Area (CALIFA) survey (Sánchez et al. 2012, 2016), which is obtaining integral field spectroscopy (IFS) for a sample of 600 nearby galaxies at  $0.005 < z < 0.03$ . The target galaxies are selected according to their angular size so that each galaxy is covered to more than two times its effective radii ( $R_e$ ) by the CALIFA integral field unit (IFU) which has a fixed field of view of  $65'' \times 72''$ . The spatial resolution of the IFU is about 390 pc per arcsec at the median redshift ( $z \sim 0.02$ ) of the sample, thus providing well resolved spectroscopy suitable for studying the bulge and bar structure of galaxies in the current work. For each galaxy CALIFA obtained IFS with two different gratings: one with a lower spectral resolution of  $R \sim 500$  and a wider wavelength coverage of 3745–7500 Å (V500), and one with a higher resolution of  $R \sim 1200$  and a narrower wavelength range of 3650–4600 Å (V1200). In this work we opt for the V500 data cubes only, in order to have measurements of the  $H\alpha$  emission line.

### 2.2. Sample selection

The CALIFA DR2 includes 200 galaxies, a random subset of the full target sample. The data was released in September, 2014 when we started this work. For each galaxy, in addition to the spectroscopic data cube, a Hubble morphological type accompanies the data release, determined by the CALIFA team based on visual examination of the optical image from the Sloan Digital Sky Survey (SDSS; York et al. (2000)). Details of the classification can be found in Walcher et al. (2014).

Figure 1 shows the CALIFA/DR2 galaxies in the plane of minor-to-major axis ratio ( $b/a$ ) versus Hubble type, where  $a$  and  $b$  are the semi-major and semi-minor axis lengths determined from SDSS  $r$ -band image by the growth curve analysis (Walcher et al. 2014). As can be seen, the sample covers all morphological types, and a wide range of inclination as well. In order to perform reliable photometric decomposition (see below), we restrict ourselves to galaxies with  $b/a > 0.5$ , thus an inclination

angle less than  $60^\circ$ . Furthermore, we've excluded galaxies with elliptical, lenticular or irregular morphology, as well as three interacting/merging systems (*NGC 5394*, *NGC 5614*, *NGC 5630*), limiting the analysis to normal spiral galaxies with regular, undisturbed morphology<sup>4</sup>. Finally, we exclude *NGC 1056*, *NGC 6314*, and *NGC 7615* because of their obvious dust lane across the optical image.

These restrictions give rise to a sample of 57 face-on spiral galaxies, of which 31 have a strong bar in the center, 9 to have a weak bar and 17 to have no obvious bar-like structure, according to the visual classification by Walcher et al. (2014). These galaxies are highlighted as solid/dark circles in Figure 1.

### 2.3. Full spectral fitting

For each spectrum in the V500 datacubes, we have performed a decomposition of the emission-line component and the stellar component (the continuum plus absorption lines) using the public code *STARLIGHT* (Cid Fernandes et al. 2004). With the emission lines being masked out, the stellar component in the observed spectrum is fitted with a model spectrum which adds up a base of 45 single stellar populations (SSPs) evenly distributed on an age-metallicity grid, with 15 ages ranging from 1 Myr to 13 Gyr and 3 different metallicities ( $Z = 0.01, 0.02, 0.05$ ). The SSPs are selected from the models of Bruzual & Charlot (2003), which were built based on the stellar library STELIB compiled by Le Borgne et al. (2003), the Padova 1994 evolutionary tracks, and a Chabrier (2003) initial mass function (IMF). The *STARLIGHT* compares the model spectra with the observed one and searches for the best-fit model through the  $\chi^2$ -minimum scheme and the Markov Chains Monte Carlo (MCMC) algorithm. Intrinsic stellar extinction is modeled as rising from the foreground dust, with the extinction law of Cardelli et al. (1989). More details about *STARLIGHT* and the BC03 models can be found in the relevant papers mentioned above. The observed spectra are corrected for Galactic extinction and resampled to have an wavelength interval of  $\Delta\lambda = 2\text{\AA}$ , before the spectral fitting. The spectral fitting is performed to each spaxel separately, without Voronoi binning. The typical S/N per spaxel depends on radius. The typical S/N of the stellar continuum in the central region,  $R_e$  and  $2R_e$  are around 40, 20 and 10, respectively. The observed spectra are well fitted, with a reduced  $\chi^2$  of 1-2 in general.

Following Li et al. (2015) and previous studies (e.g. Kauffmann et al. 2003), we use  $D_n(4000)$  and the equivalent width of  $H\delta$  absorption line,  $EW(H\delta_A)$ , as indicators of the recent star formation history. It is well known that  $D_n(4000)$  is a good proxy for the stellar age below  $\sim 2$  Gyr, and  $H\delta_A$  a sensitive tracer of the star formation that happened 0.1-1 Gyr ago (Bruzual & Charlot 2003). In addition, we use the equivalent width of  $H\alpha$  emission line,  $EW(H\alpha)$ , as an indicator of the current star formation activity. For each spaxel in the data cubes we measure  $D_n(4000)$  and  $EW(H\delta_A)$  from the best-fit spectrum, adopting the definition of the two parameters introduced

<sup>4</sup> We keep one galaxy (*NGC 3106*) which display slightly disturbed image in the optical, but still show quite regular morphology. See Section 4.1 for further discussion.

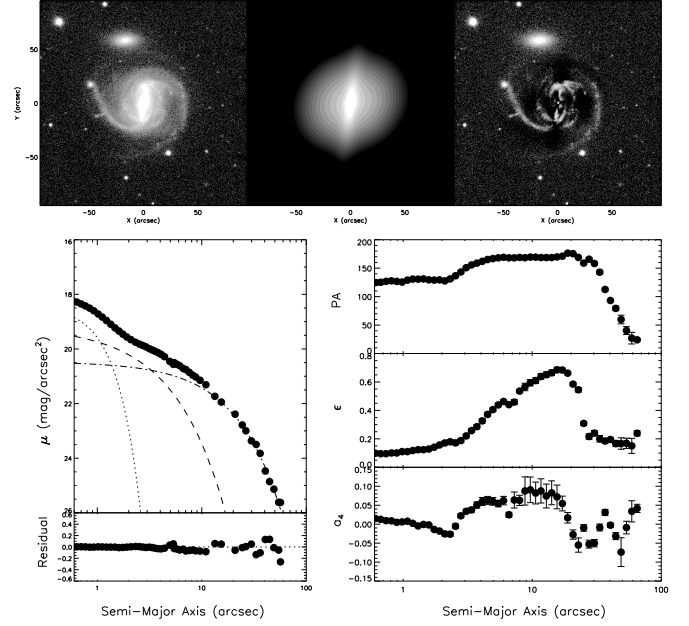


FIG. 2.— An example of photometric decomposition (*NGC 5000*). The top three panels (from left to right) show the original SDSS  $r$ -band image, the model image and the residual from GALFIT. The bottom left panel shows the one-dimensional surface brightness profiles (upper) and the data-to-model ratio (lower). The dotted, dashed and dash-dotted lines represent the bulge/bar/disk components of the GALFIT model. The bottom-right panels show the position angle, the ellipticity and the  $a_4$  parameter given by the IRAF/ELLIPSE analysis. See text for more details.

in Balogh et al. (1999) and Worthey & Ottaviani (1997).  $EW(H\alpha)$  is measured by fitting a single Gaussian profile to the pure emission line spectrum, obtained by subtracting the best-fit stellar component from the observed one.

We'd like to point out that, although *STARLIGHT* provides quantitative measurements of mean stellar age, in the rest of this paper we will mostly use the three diagnostic parameters, that is,  $D_n(4000)$ ,  $EW(H\delta_A)$  and  $EW(H\alpha)$ . In particular, we will use relative measurements of the three indices and concentrate on their radial profiles and gradients. In most cases we do not present the derived measurements of stellar age, to avoid potential effect of the known issues in current stellar population synthesis models, such as the degeneracy between age, metallicity and dust, and the uncertainty in IMF. However, as we will show at the end of the paper, our conclusions based on the three indices are in good agreement with those from the stellar age measurements. The typical errors for  $D_n(4000)$ ,  $EW(H\delta_A)$  and  $\lg(EW(H\alpha))$  in spaxels of SNR=10 are 0.11, 1.05  $\text{\AA}$  and 0.15 dex, respectively.

### 2.4. Photometric decomposition

We have performed a careful, photometric decomposition of the bulge and disk components for all the 57 face-on spirals in our sample. For barred galaxies we also include the bar structure as a third component in the decomposition. The decomposition is performed on the SDSS  $r$ -band image. We download the original images from the SDSS DR7 Data Archive Server, and we determine the sky background and mask out foreground



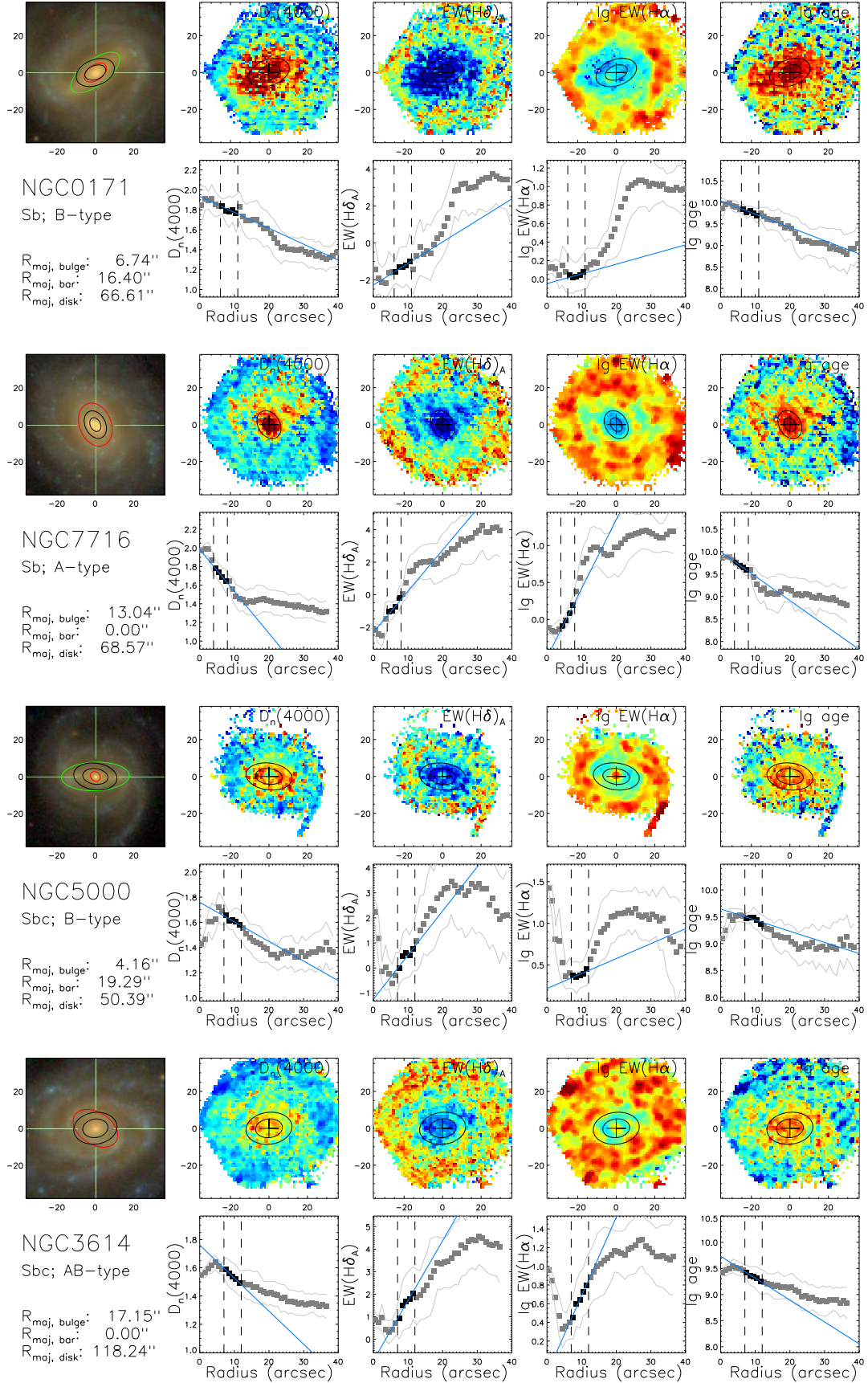


FIG. 3.— Optical *gri* image (left column) and maps/profiles of  $D_n(4000)$ ,  $EW(H\delta_A)$ ,  $EW(H\alpha)$  (column 2-4) and stellar age (right column) are shown for four example galaxies in our sample (from top to bottom): NGC 0171, NGC 7716, NGC 5000 and NGC 3614. In each image the red and green ellipse indicates the radius of the bulge and (if available) bar. The two black ellipses indicate the radial range in which we perform the linear fit to the radial profile, as also indicated as the two vertical dashed lines in the panels of the radial profiles, where the linear fit is plotted as the blue line.

stars and neighboring sources, in the same way as described in [He et al. \(2013\)](#).

As mentioned above, visual identification of bars is done for the CALIFA galaxies. For this work we re-do the identification by applying the IRAF task **ELLIPSE** to the background subtracted image of each galaxy in our sample. The **ELLIPSE** fits elliptical annuli to surface brightness isophotes at logarithmically increased radii, and simultaneously determines a one-dimensional radial profile for the ellipticity, the position angle of the major axis, and the surface brightness. Following [Barazza et al. \(2008\)](#), we identify the bar structure according to the presence of an abrupt drop in the ellipticity profile: a galaxy is classified to have a bar if the ellipticity increases above 0.25 as one goes from galactic center outwards and then drops by at least 0.1 at some radius. As a result, 32 of the 57 galaxies in our sample are classified as barred, of which 29 are visually identified as barred (B-type) and 3 as unknown type (AB-type) in the CALIFA/DR2. We will use our classification for the rest of this paper. Indeed we have repeated all the analysis using the classification from the CALIFA/DR2 and found all our conclusions to remain the same.

For each galaxy we perform a two-dimensional decomposition by applying the public code **GALFIT** ([Peng et al. 2002](#)) to the  $r$ -band SDSS image, with either a two component model (bulge+disc) if the galaxy doesn't have a bar, or a three component model (bulge+bar+disc) if it is barred. The disc component is characterized by an exponential profile, while both the bulge and bar components are described by a Sérsic profile. The model is convolved with the point spread function determined from the observed image, in order to take into account the effect of seeing. Parameters of the different components of the best-fit model are listed in Table 1.

As an example, Figure 2 shows the observed, best-fit and data-to-model residual images for one of our galaxies, *NGC 5000*, as well as the one-dimensional profiles of the bulge, disc and bar components from the model. The **ELLIPSE**-based profiles are also shown, which are used to identify the presence of the bar component in the galaxy. In the last column of Table 1 we list the reduced  $\chi^2$  of the model fits, which are mostly at  $\sim 1 - 2$  indicating that the images are well fitted with these models.

From the best-fit models, we determine the sizes of bulge/bar/disk as the radius at which the surface brightness is equal to  $25.0 \text{ mag arcsec}^{-2}$ . These radii will be used for the analysis below.

### 3. RESULTS

#### 3.1. 2D maps and radial profiles of $D_n(4000)$ , $EW(H\delta_A)$ and $EW(H\alpha)$

For each of the 57 galaxies in our sample, we first obtain the two-dimensional (2D) maps of the three diagnostic parameters,  $D_n(4000)$ ,  $EW(H\delta_A)$  and  $EW(H\alpha)$ , from which we then estimate the radial profiles of the same parameters. When constructing these profiles, we have corrected for the effects of inclination on the radius for each spaxel in the datacubes, using the global ellipticity, the position angle of the major axis and the major-to-minor axis ratio from the CALIFA data release ([Walcher et al. 2014](#)), and adopting a constant spatial sampling of  $1''$  along the major axis and fixed ellipticity and position

angle for all the radial bins. In Figure 3 we present the 2D maps and the radial profiles for four example galaxies, of which two are barred galaxies (*NGC 0171*, *NGC 5000*) and two are unbarred (*NGC 7716*, *NGC 3614*). We also show the SDSS *gri* image and the maps/profiles of stellar age given by **STARLIGHT**.

An overall impression from the 2D maps is that all the galaxies in our sample display spatial variation in all the three parameters, though to varying degrees and to differing radial extents. We find that, in general, the galaxies in our sample show larger  $D_n(4000)$ , as well as smaller  $EW(H\delta_A)$  and  $EW(H\alpha)$  in the inner region than in the outer regions. These general trends are consistent with what have been found for spiral galaxies from optical imaging, where a spiral galaxy typically displays a red, dense bulge in the center, surrounded by bluer, more diffuse light in/between spirals at larger radii. These results also echo the previous studies of the stellar population gradients based on stellar population synthesis applied to the CALIFA datacubes (e.g. [Pérez et al. 2009](#); [Sánchez-Blázquez et al. 2011](#)).

When compared to the 2D maps, the radial profiles reveal these trends in a more compact and quantitative manner:  $D_n(4000)$  typically shows a negative slope over the entire galaxy, while both  $EW(H\delta_A)$  and  $EW(H\alpha)$  show positive slopes. We see that the profile of  $D_n(4000)$  can be divided into two parts in most cases: an inner part which can be described by a linearly decreasing function, and an outer part which is also linear but usually flatter than the inner part. The  $EW(H\delta_A)$  and  $EW(H\alpha)$  profiles can be similarly divided into two parts with a linear inner part, but the outer part displays more fluctuations. The dividing radius between the two parts changes from galaxy to galaxy, but it appears to occur at the radius which separates the central bulge/bar from the outer spirals. The fluctuant outer profiles of  $EW(H\delta_A)$  and  $EW(H\alpha)$  are consistent with both the clumpy, highly structured outskirts of their 2D maps, and the spiral/clumpy light distribution in the optical image. In contrast, the map of  $D_n(4000)$  looks pretty smooth in the same regions. As indicators of current and very recent star formation, both  $EW(H\alpha)$  and  $EW(H\delta_A)$  are expected to be strong only in strong star forming regions (HII regions) which are discretely distributed in the spirals of galaxies. The  $D_n(4000)$  indicates relatively older stellar populations, formed over the past 1-2 Gyr, so it is not surprising to see a smoother distribution of this parameter.

#### 3.2. The central “turnover” in $D_n(4000)$ , $EW(H\delta_A)$ and $EW(H\alpha)$ profiles

In this subsection we will concentrate on the inner region of our galaxies where a bulge and (sometimes) a bar are identified, aiming to examine the recent star formation history in the central bulge, and in particular the role of the bar structure in this regard.

As described above, in most of our galaxies the inner region can be described by a linear profile, with a negative radial gradient in  $D_n(4000)$  and positive gradients in  $EW(H\delta_A)$  and  $EW(H\alpha)$ . In some of our galaxies, thanks to its high spatial resolution, the CALIFA data reveals a “turnover” in the inner-most region, where the three diagnostic parameters significantly deviate from the featureless, linear profile. This can be seen from the

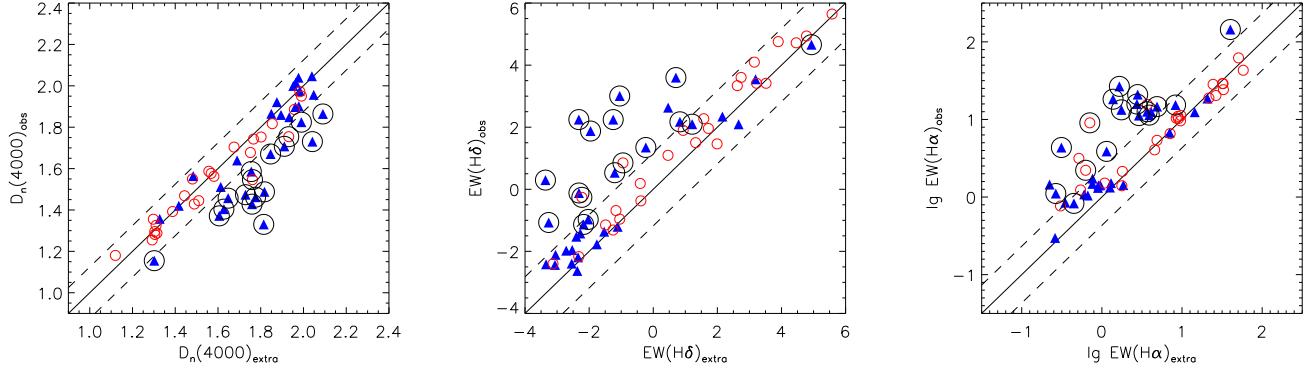


FIG. 4.— Comparison between the observed central values and the inward extrapolated values for the three diagnostic parameters (from left to right):  $D_n(4000)$ ,  $EW(H\delta_A)$  and  $EW(H\alpha)$ . Barred and unbarred galaxies are plotted separately as solid blue triangles and red open circles. The turnover galaxies identified by the  $D_n(4000)$  profile are highlighted with a big black circle. The solid line is the 1 : 1 relation, and the two dashed lines indicate the  $1\sigma$  scatter of all the galaxies around the 1 : 1 relation.

maps/profiles of *NGC 5000* and *NGC 3614*, the lower two galaxies shown in Figure 3. In both galaxies, the profile of  $D_n(4000)$  has a negative slope at radii larger than  $\sim 5''$ , but exhibits a significant drop at smaller radii. Similarly, an upturn is seen in both  $EW(H\delta_A)$  and  $EW(H\alpha)$ , also in the inner-most region of the two galaxies. The other two galaxies, *NGC 0171* and *NGC 7716* as shown in the upper two rows of the same figure, do not show a significant “turnover” in either  $D_n(4000)$  or  $EW(H\delta_A)$ , whereas a similar but weaker upturn is noticeable in  $EW(H\alpha)$ , also in the very center of the galaxy.

In order to quantify the “turnover” feature, for each galaxy, we first determine an outer radius of its central region,  $R_{out}$ , according to the photometric decomposition described in 2.4. We define  $R_{out}$  as the radius along major axis where the  $r$ -band surface brightness  $\mu_r$  falls below  $25 \text{ mag arcsec}^{-2}$ , in either the best-fit bulge component (for unbarred galaxies) or the best-fit bar component (for barred galaxies)<sup>5</sup>. We also determine an inner radius,  $R_{in}$ , which is set to  $3''$  for unbarred galaxies, or  $R_{25,bulge}$  if the galaxy has a bar. Here,  $R_{25,bulge}$  is the radius along major axis at which the  $r$ -band surface brightness of the bulge component reaches  $25 \text{ mag arcsec}^{-2}$ . We then fit a linear function to the observed profiles of all the three diagnostic parameters over the radial range  $(R_{in} + R_{out})/2 \pm 2''$ , i.e. using the middle 5 data points in the radial range of  $R_{in} < R < R_{out}$ . Actually we have also done the fitting using all the data points falling in between  $R_{in}$  and  $R_{out}$ , but finding the two radii to cover a part of the spiral arms or the central turnover region in some cases. In practice, we find that the middle 5 data points provide a good enough fit to the overall profile in the central region, with little contaminations from the transition regions. For comparison we have performed the linear fit also to the stellar age profile derived from *STARLIGHT*. In Figure 3 the linear fits are shown as a blue solid line for each profile. The 5 data points used for the fitting are highlighted as black squares, and the two vertical dashed lines indicate the

lower and upper radii of these data points.

The “turnover” of a given parameter is then quantified by comparing the observed value in the central spaxel with the value at  $R = 0$  as extrapolated from the best-fit linear profile. Figure 4 presents this comparison for the three parameters. In each panel, the black solid line indicates the 1 : 1 relation, and the two dashed lines the  $1 - \sigma$  scatter ( $0.14$ ) of the galaxies around this relation. We plot barred and unbarred galaxies as blue triangles and red circles separately. The differing behavior of the two classes is striking. The majority of the unbarred galaxies follow well the 1 : 1 relation, whereas a large fraction of the barred galaxies deviate significantly from that relation, i.e., falling below the lower dashed line. Specifically, the fraction of barred galaxies with significant turnover in  $D_n(4000)$ ,  $EW(H\delta_A)$  and  $EW(H\alpha)$  are  $15/32$ ,  $13/32$  and  $14/32$ , respectively.

We define a galaxy to be a “turnover” galaxy if it presents a significant turnover feature in  $D_n(4000)$ , that is, falling below the lower  $1 - \sigma$  line in the left-most panel of Figure 4. Out of the 57 galaxies in our sample, 17 are classified as “turnover”. These galaxies are highlighted as big circles in every panel of the figure. We see that, most of the turnover galaxies defined by the  $D_n(4000)$  also show turnover feature in the other two parameters. Table 2 lists the observed and extrapolated values of the central  $D_n(4000)$ , as well as the slope of the inner  $D_n(4000)$  profile derived from the linear fit. Table 3 lists the number of turnover galaxies identified according to  $D_n(4000)$ ,  $EW(H\delta_A)$  and  $EW(H\alpha)$  profiles.

A striking result that one can immediately identify from this figure is that, all but two of the turnover galaxies have a bar structure. Considering that the turnover is observed in only about half of the barred galaxies, our finding suggests that the presence of a bar is a necessary, but not sufficient condition for a galaxy to show the turnover feature. The fact that most of our turnover galaxies consistently show the turnover feature in all the three parameters can be regarded as clear signature of recent and ongoing star formation in their central region. Therefore, our results provide direct evidence for the central star formation as induced by bar-driven instabilities.

It is interesting to note that, the turnover galaxies are dominated by those galaxies which have intermediate *observed* values of the diagnostic parameters. In consis-

<sup>5</sup> We note that, at  $R_{out}$ , the bar component (if applicable) is exclusively much stronger than the bulge component, and using the total surface brightness of both components instead of the bar component alone doesn’t change  $R_{out}$ , nor the analyses in the rest of the paper.



tent with this, the barred galaxies without a turnover feature show bi-modal distributions in these parameters. For instance, they can be well separated into two groups according to  $D_n(4000)$ : one with the largest  $D_n(4000)$  ( $D_n(4000) > 1.8$ , thus dominated by old stellar populations), and one with very small  $D_n(4000)$  ( $D_n(4000) < 1.6$ , thus indicative of stellar populations younger than 1-2 Gyr). Such bi-modal distribution gives rise to a gap in a given parameter, both observed and extrapolated, for the barred galaxies with no turnover. Our result implies that, the barred galaxies with a central bulge of intermediate stellar ages are more unstable to bar-driven instabilities, when compared to those with either old or young bulges.

### 3.3. Global properties of the turnover galaxies

In this subsection we will examine the global properties of the turnover galaxies, including their stellar mass ( $M_*$ ), NUV-to-optical color (NUV- $r$ ), concentration index ( $R_{90}/R_{50}$ ), HI gas fraction ( $\lg(M_{\text{HI}}/M_*)$ ) and nuclear activity. We take estimates of  $M_*$ , NUV- $r$  and  $R_{90}/R_{50}$  from the version v0.1.2 catalog of NASA-Sloan Atlas (NSA) <sup>6</sup>, which is a catalog of images and parameters of local galaxies based on data from SDSS (York et al. 2000), GALEX (Martin et al. 2005) and 2MASS (Skrutskie et al. 2006); see Blanton et al. (2005a,b, 2011) for details. The stellar mass of each galaxy is estimated by Blanton & Roweis (2007) from the SDSS five-band Petrosian magnitudes. NUV- $r$  is given by the integrated light in the NUV band from GALEX and the  $r$ -band Petrosian magnitude from SDSS. Both are corrected for Galactic extinction. The concentration index is defined as the ratio of  $R_{90}$  to  $R_{50}$ , the radii enclosing 90% and 50% of the total light in the SDSS  $r$ -band image. Furthermore, the HI gas masses have been collected from HyperLeda database (Makarov et al. 2014) <sup>7</sup>. A part of galaxies are covered by ALFALFA survey (Haynes et al., in preparation; results for 70% coverage) <sup>8</sup>. Since the errors of HI fluxes from ALFALFA are smaller, we replaced the ALFALFA HI measurements for the overlapped sources.

Figure 5 displays the global properties of our galaxies: NUV- $r$  versus  $\lg(M_*/M_\odot)$ ,  $R_{90}/R_{50}$  versus  $\lg(M_*/M_\odot)$ , and  $\lg(M_{\text{HI}}/M_*)$  versus  $\lg(M_*/M_\odot)$ , highlighting the barred, unbarred and turnover galaxies with the same symbols/colors as in the previous figure. For comparison, we have selected a volume-limited sample of 35070 galaxies with stellar mass above  $10^8 M_\odot$  and redshift in the range  $0.01 < z < 0.03$  from the NSA. Distributions of this sample are plotted in grayscale maps in both panels. When compared to the SDSS sample, the CALIFA mother sample lacks galaxies of low mass, particularly for the red population. However, as can be seen from the figure, the CALIFA sample is still representative of the general population at masses above  $\sim 10^{10} M_\odot$  (see Walcher et al. 2014 for a more quantitative demonstration). As expected, the CALIFA galaxies are well separated into the red sequence with NUV- $r > 5$  and the blue cloud with NUV- $r < 4$ , with a minority of the sample falling in the green valley in between.

Most of the galaxies in our sample are located in the blue cloud and green valley in the color-mass diagram, and have concentration indices smaller than  $R_{90}/R_{50} = 2.6$ , indicative of late-type morphologies. This is expected as our sample is limited to spiral galaxies by selection. The unbarred galaxies in our sample are preferentially found in the blue cloud, with only a few extending to the green valley. In contrast, the barred galaxies are distributed over both the green valley and blue cloud regions. Looking at the barred galaxies only, we find the galaxies with and without turnover feature to show quite distinct distributions in the color-mass diagram — the non-turnover galaxies mostly fall in the green valley, but the turnover population is biased towards the blue cloud. The same trends/differences are not seen in the  $R_{90}/R_{50}$ - $\lg(M_*/M_\odot)$  diagram, where the different types of galaxies appear to occupy similar regions.

In Figure 6 we present the  $D_n(4000)$ - $\lg(M_*/M_\odot)$  diagram which plots the  $D_n(4000)$  as measured from the central region of the galaxies as a function of their total stellar mass. For the background SDSS sample and the CALIFA mother sample, we take the  $D_n(4000)$  measurements from the NSA which are based on the SDSS 3''-fiber spectra. Since SDSS spectroscopy is available only for half of the selected 57 face-on spiral galaxies, for these galaxies we instead plot the  $D_n(4000)$  measured from the central spaxel of their CALIFA datacubes. We note that the CALIFA samples, both the mother sample and the subset studied here, appear to lack galaxies with highest  $D_n(4000)$  compared to the SDSS sample, although the CALIFA samples do include galaxies of highest NUV- $r$  colors. We have compared the  $D_n(4000)$  as obtained from the SDSS and the CALIFA central spaxel for a sample of CALIFA/DR2 galaxies with data available from both surveys. The two measurements agree well, but the IFU central spaxel gives a value that is slightly larger than the value from the SDSS 3''-fiber, with difference of  $\Delta D_n(4000) \sim 0.05$ . This means the lack of galaxies with highest  $D_n(4000)$  is indeed the case for the CALIFA samples, and this cannot be attributed to this slight difference between the CALIFA and SDSS measurements. The slight difference may be a combined effect of the possible errors in fiber centroiding and seeing/resolution effect (Sánchez et al. 2012), as well as the negative gradient of the  $D_n(4000)$  profiles of galaxies. Nevertheless, this small effect is neglectable for the comparisons of the different samples presented here.

Similar to the NUV- $r$ - $\lg(M_*/M_\odot)$  diagram, the turnover galaxies are observed to be located in the young population regions which can be defined by  $D_n(4000) < 1.6$ , while the barred galaxies without turnover feature mostly have  $D_n(4000) > 1.6$ . When plotted using the extrapolated  $D_n(4000)$  (the middle panel), the turnover galaxies are located mostly above the empirical divider of  $D_n(4000) = 1.6$ . As a result, the barred galaxies as a whole are largely confined to the area of old populations, with only a few galaxies scattering towards the young population region. A reasonable conjuncture based on our result is that, most barred galaxies in our sample had their central star formation quenched at an earlier time, but for some reason some of these galaxies (the turnover galaxies) recently experienced, or is experiencing a new round of star formation, thus moving from the old population region back to the young population region in the

<sup>6</sup> NSA: <http://www.nsatlas.org>

<sup>7</sup> HyperLeda: <http://leda.univ-lyon1.fr/>

<sup>8</sup> ALFALFA: <http://egg.astro.cornell.edu/alfalfa/>

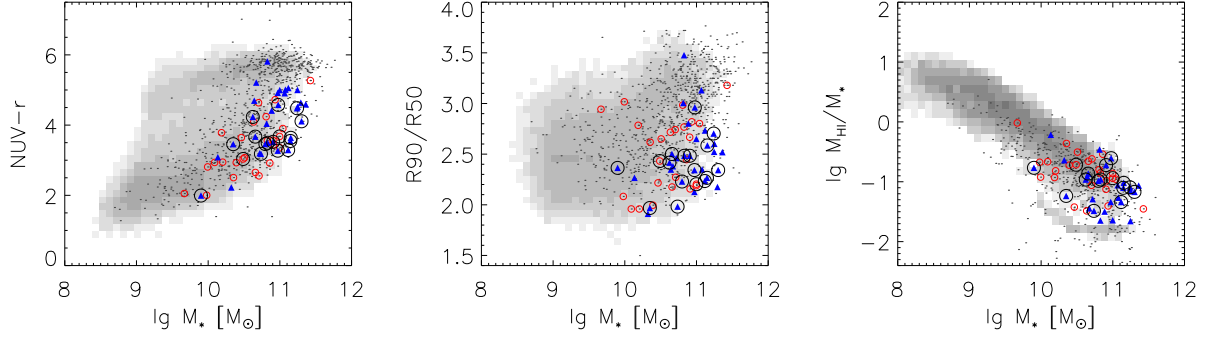


FIG. 5.— The 57 face-on spiral galaxies studied in this work are plotted as red circles (unbarred galaxies) or blue triangles (barred galaxies), on the  $\text{NUV-}r$ - $\lg(M_*/M_\odot)$  plane (left panel),  $R_{90}/R_{50}$ - $\lg(M_*/M_\odot)$  plane (middle panel), and  $\lg(M_{\text{HI}}/M_*)$ - $\lg(M_*/M_\odot)$  plane (right panel). The galaxies with significant turnover in the central  $D_n(4000)$  (see text for details) are highlighted as large black circles. Plotted in small dots are the 939 galaxies in the CALIFA mother sample. Distributions of a volume-limited sample selected from the SDSS are shown as gray scale for comparison.

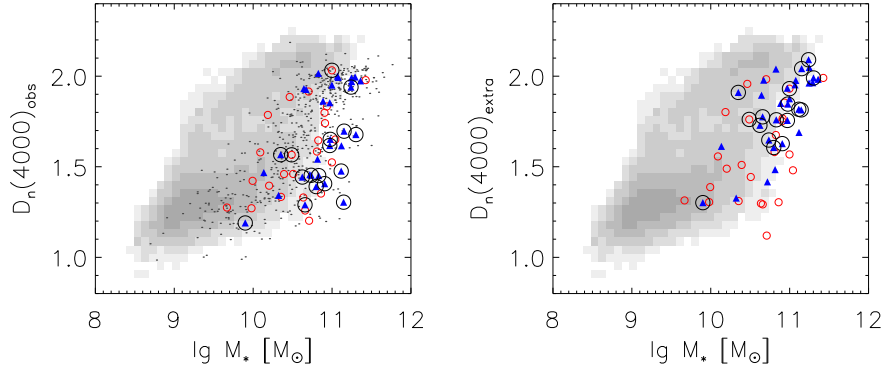


FIG. 6.— The 57 face-on spiral galaxies studied in this work are plotted on the diagram of central  $D_n(4000)$  versus stellar mass, with the same symbols/colors as in the previous figure. For the galaxies with a  $D_n(4000)$  turnover feature, the left (right) panel plots the observed (extrapolated) value of the central  $D_n(4000)$  (see text for details). The grayscale maps and small dots present the SDSS sample and the CALIFA mother sample, for comparison.

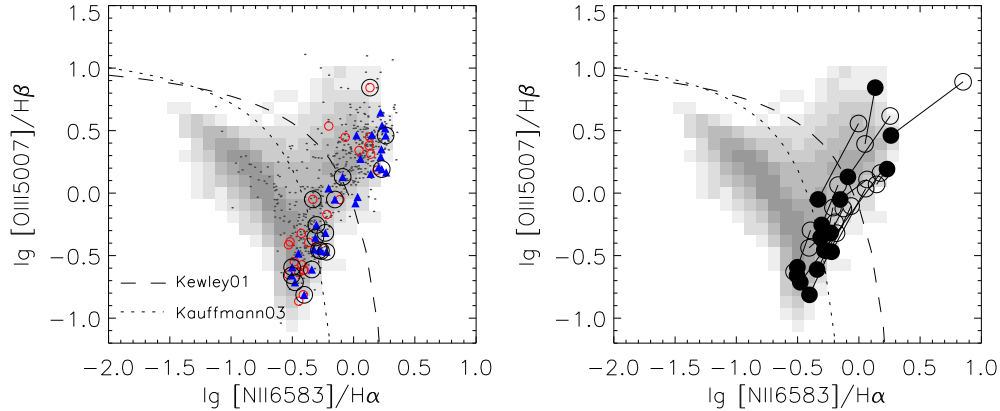


FIG. 7.— In the left panel the 57 face-on spiral galaxies studied in this paper are plotted on the BPT (Baldwin et al. 1981) diagram, using the same symbols/colors as in Figure 5. The relevant emission line fluxes are measured from the central spaxel of the CALIFA IFU. The right panel presents the BPT diagram for the turnover galaxies only, but showing the results for both the observed emission line fluxes (filled circles), and the fluxes from inward extrapolating the linear fit of the emission line flux profiles (open circles). For each galaxy the observed and extrapolated values are connected by a solid line. Distributions of a volume-limited sample of galaxies selected from SDSS are shown as grayscale maps in both panels, and 939 galaxies from the CALIFA mother sample are plotted small dots in the left panel, for comparison.

$D_n(4000)$ - $\lg(M_*/M_\odot)$  diagram.

Figure 7 presents our samples on the BPT diagram (Baldwin et al. 1981). The fluxes of the four relevant emission lines are measured either from the SDSS 3''-

fiber spectra for the SDSS sample, or from the central spaxel of the CALIFA datacubes for both the CALIFA mother sample and the 57 galaxies studied here. As can be seen from the left panel, our sample cover a



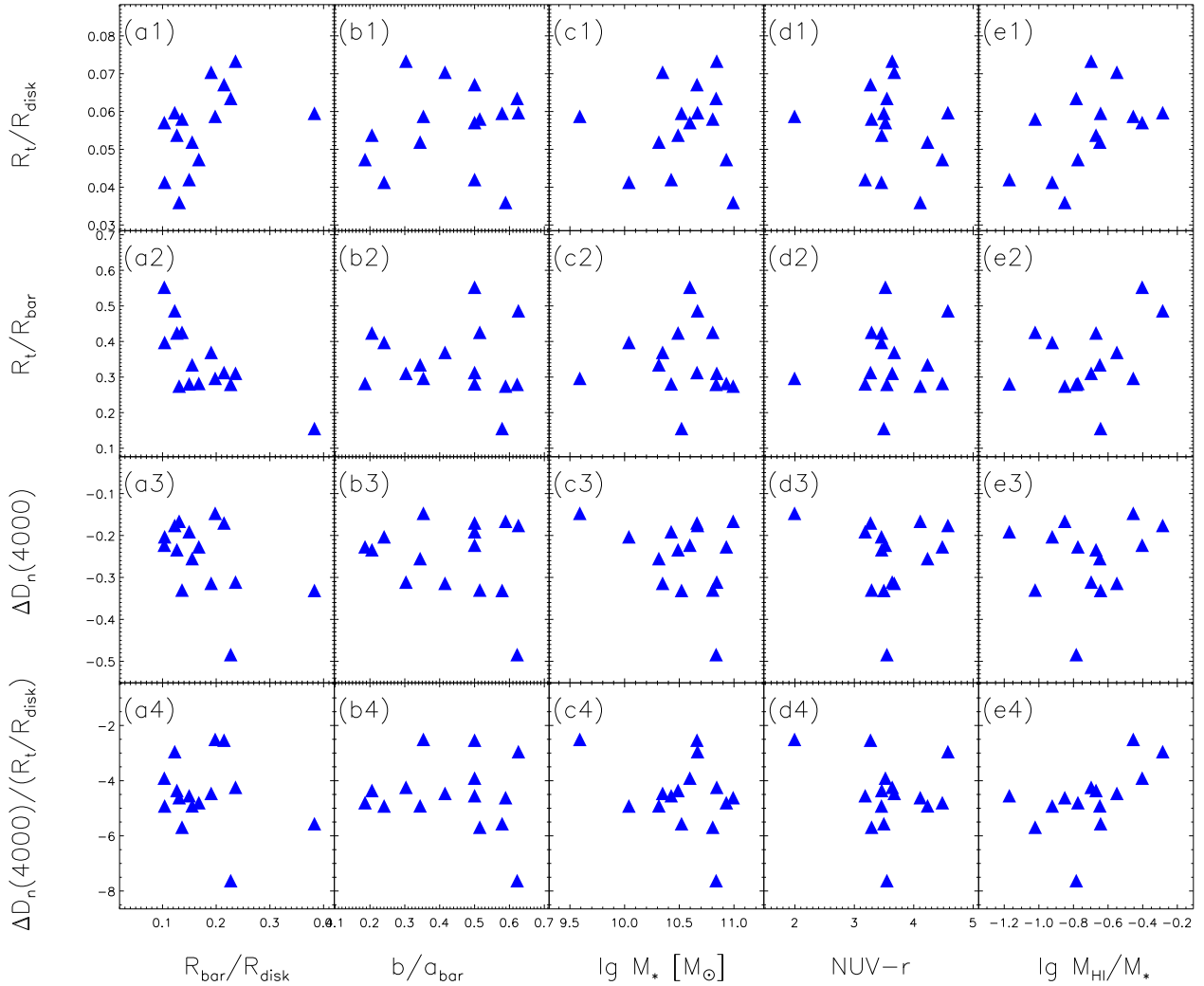


FIG. 8.— The size and strength of the turnover region are plotted as a function of galaxy properties. The y-axis of panels from top to bottom shows the turnover-to-disk radius ratio ( $R_t/R_{\text{disk}}$ ), the turnover-to-bar radius ratio ( $R_t/R_{\text{bar}}$ ), the drop in central  $D_n(4000)$  ( $\Delta D_n(4000)$ ) and the turnover strength-to-size ratio ( $\Delta D_n(4000)/(R_t/R_{\text{disk}})$ ). The x-axis of panels from left to right is the bar-to-disk radius ratio ( $R_{\text{bar}}/R_{\text{disk}}$ ), the minor-to-major axis ratio of the bar ( $b/a_{\text{bar}}$ ), stellar mass ( $\lg(M_*/M_\odot)$ ) and the NUV- $r$  color.

wide area in the BPT diagram, including star-forming, AGN/SF composite, and AGN host galaxies, although the sample lacks both Seyferts and strongly star-forming galaxies due to the lack of low-mass galaxies in the CALIFA survey. The distributions of barred and unbarred galaxies are similar, consistent with previous findings that the presence of a prominent bar is not closely linked to the nuclear activity of galaxies (e.g. Lee et al. 2012; Cheung et al. 2015). It is interesting that, although the barred galaxies as a whole are distributed over all the three regions on the BPT diagram, those falling in the AGN region are mostly non-turnover galaxies, while the turnover galaxies are predominantly found in the star-forming and composite regions. Among the 17 turnover galaxies, the number of galaxies in the AGN/composite/SF regions are 4, 8, 5, respectively. For the 15 non-turnover barred galaxies, only two are located outside the AGN region, with one composite and one SF

galaxy.

The distinct behavior of the turnover and non-turnover galaxies on the BPT diagram is not surprising, if the turnover in the SFH diagnostic parameters is a result of the central star formation caused by the bar-driven gas inflow. In this case, the emission line fluxes of the central region used for the BPT diagram may also deviate from their normal values, thus leading the galaxy to move to a different location on the diagram. To test this hypothesis, we have measured the profiles for the four emission lines and quantify the central turnover feature in the same way as we did for the three SFH diagnostic parameters. In the right-hand panel of Figure 7 we plot the turnover galaxies, i.e. those identified according to the  $D_n(4000)$  profile, using both the observed emission line fluxes (filled circles) and the fluxes obtained from extrapolating the linear fit profile (open circles). All the galaxies move their location, though to varying degrees.

This confirms that the relevant emission lines also show turnover feature in the galactic center, like what we find for the SFH diagnostic parameters, and bar-driven gas inflow can well be the physical process driving all these turnover features.

### 3.4. Correlations of the turnover feature with host galaxy properties

In the previous subsection we have examined the global properties of the turnover galaxies. In this subsection we will characterize the turnover feature and examine the correlation with host galaxy properties.

For each turnover galaxy, we estimate two quantities,  $\Delta D_n(4000)$  and  $R_t$ , to respectively characterize the strength and size of the turnover feature. Here,  $\Delta D_n(4000)$  is defined as the difference of the observed  $D_n(4000)$  in the central spaxel relative to the central  $D_n(4000)$  obtained from extrapolating the linear fit. The radius of the turnover region,  $R_t$ , is determined from the  $D_n(4000)$  profile of a given galaxy, defined to be the maximum radius along major axis beyond which the observed  $D_n(4000)$  no longer deviates significantly from the linear fit (see §3.2). We also determine the radius for both the disk component ( $R_{\text{disk}}$ ) and (when applicable) the bar component ( $R_{\text{bar}}$ ), the radius along major axis where the disk or bar component of the surface brightness profile drops to 25 mag arcsec<sup>-2</sup> (see §2.4). We use  $R_t/R_{\text{disk}}$  and  $R_t/R_{\text{bar}}$  to describe the relative size of the turnover with respect to the disk and bar components, and  $\Delta D_n(4000)/R_t$  to indicate the specific turnover strength per unit radius. In Figure 8 we show the turnover properties including turnover size relative to both disk and bar sizes ( $R_t/R_{\text{disk}}$ ,  $R_t/R_{\text{bar}}$ ), turnover strength ( $\Delta D_n(4000)$ ) and strength-to-size ratio ( $\Delta D_n(4000)/(R_t/R_{\text{disk}})$ ), as a function of host galaxy properties including bar-to-disk radius ratio ( $R_{\text{bar}}/R_{\text{disk}}$ ), minor-to-major axis ratio of the bar ( $b/a_{\text{bar}}$ ), stellar mass ( $\lg(M_*/M_\odot)$ ), NUV- $r$  color and H I gas fraction ( $\lg(M_{\text{HI}}/M_*)$ ).

Both the turnover size and its strength are not correlated with galaxy mass or color. And there are no clear correlations with the bar ellipticity as quantified by the minor-to-major axis ratio of the bar. The probable weak correlations can be only seen from bar length (the first column *a*) and H I gas fraction (the last column *e*). As seen in panel *a1*,  $R_t/R_{\text{disk}}$  is positively correlated with  $R_{\text{bar}}/R_{\text{disk}}$ , that is, galaxies with longer bars tend to have larger area of turnover feature in their central region when compared to the galaxies with similar disk size but shorter bars. A similar correlation between turnover size and disk size can be seen from panel *a2*, although the correlation is mainly contributed by a few galaxies with highest  $R_t/R_{\text{bar}}$  but lowest  $R_{\text{bar}}/R_{\text{disk}}$ . This might be suggesting that, although the bar size is more closely linked with the turnover size, for galaxies with similar sizes of bars, they may also have larger turnover area if their disks are larger. As for the H I gas fraction, both  $R_t/R_{\text{disk}}$  and  $\Delta D_n(4000)/(R_t/R_{\text{disk}})$  are larger as the increasing of H I gas fraction. It suggests that the turnover size and its strength correlate with the amount of gas in the disk. If there is enough gas supply, the central star formation can be supported for long timescale. Unfortunately, we did not find any CO measurements

of our galaxies from the current databases. The direct observational evidences are still needed to confirm this.

### 3.5. Recent star formation histories of the turnover galaxies

In Figure 9 we display our galaxies on the diagnostic diagrams of recent star formation history, namely the planes of  $D_n(4000)$  versus  $\text{EW}(\text{H}\delta_A)$  (upper panels) and  $\text{EW}(\text{H}\delta_A)$  versus  $\text{EW}(\text{H}\alpha)$  (lower panels). In the left two columns we show all the galaxies in our sample, but for the turnover galaxies, we use the observed parameters in the first column and the extrapolated parameters in the second. The barred, unbarred and turnover galaxies are plotted with blue triangles, red small circles and black big circles. In the right-most column we display the turnover galaxies only, showing both the observed and extrapolated values which are connected by a solid line for a given galaxy. For comparison and in each panel, we present the same parameters for the solar-metallicity models of BC03 that follow exponentially declining star formation histories, with solid lines for continuous star formation decline with long  $e$ -folding times ( $\tau > 5 \times 10^8 \text{yr}$ ) and dashed lines for bursts of star formation with fairly short  $e$ -folding time ( $\tau < 5 \times 10^8 \text{yr}$ ). The  $D_n(4000)$  and  $\text{EW}(\text{H}\delta_A)$  indices are measured from the BC03 model spectra adopting the same definitions as the observed spectra. For  $\text{EW}(\text{H}\alpha)$ , we compute a  $\text{H}\alpha$  luminosity from the output of each BC03 model, by converting Lyman continuum photons to  $\text{H}\alpha$  photons following Hunter & Elmegreen (2004) (see Equations (B2)-(B4) in their Appendix) and adopting the recombination coefficients and  $\text{H}\alpha$ -to- $\text{H}\beta$  ratios from Hummer & Storey (1987). We assume nebular temperatures of  $T_e = 15,000, 10,000$ , and  $5000\text{K}$  for the LMC, solar-metallicity, and supersolar-metallicity models, respectively.

Overall, our sample occupies roughly the same region as the models of continuum star formation decline in both  $D_n(4000)$ - $\text{EW}(\text{H}\delta_A)$  and  $\text{EW}(\text{H}\delta_A)$ - $\text{EW}(\text{H}\alpha)$  planes, with no galaxies falling in the region of star formation bursts. The unbarred sample covers full ranges in all the three parameters. When plotted with the observed parameters, the barred sample lacks galaxies with lowest  $D_n(4000)$ , highest  $\text{EW}(\text{H}\delta_A)$ , and highest  $\text{EW}(\text{H}\alpha)$ . When the turnover galaxies are plotted using the extrapolated instead of the observed parameters, the barred galaxies are mostly located in the regions of low- $D_n(4000)$ , high- $\text{EW}(\text{H}\delta_A)$  and high- $\text{EW}(\text{H}\alpha)$ , consistent with models which contain no/little young populations and haven't experienced star formation in the past 1-2 Gyr. The difference between the first and second columns is caused by the turnover galaxies which are observed to be located in the intermediate regions and move to the low- $D_n(4000)$  and high- $\text{EW}(\text{H}\delta_A)$  region when plotted with the extrapolated values. The systematic change of their locations is seen more clearly in the right-most panels which show the turnover galaxies only, but using both the observed and the extrapolated values.

In Figure 10 (upper panels), we plot the slope of the  $D_n(4000)$  profile obtained in §3.1 by fitting a linear function to the inner region, as a function of the observed (left) and extrapolated (middle) central  $D_n(4000)$  (middle), and the difference between the two indices (right). All the galaxies except one present a negative or flat slope. For unbarred galaxies (red open circles), the

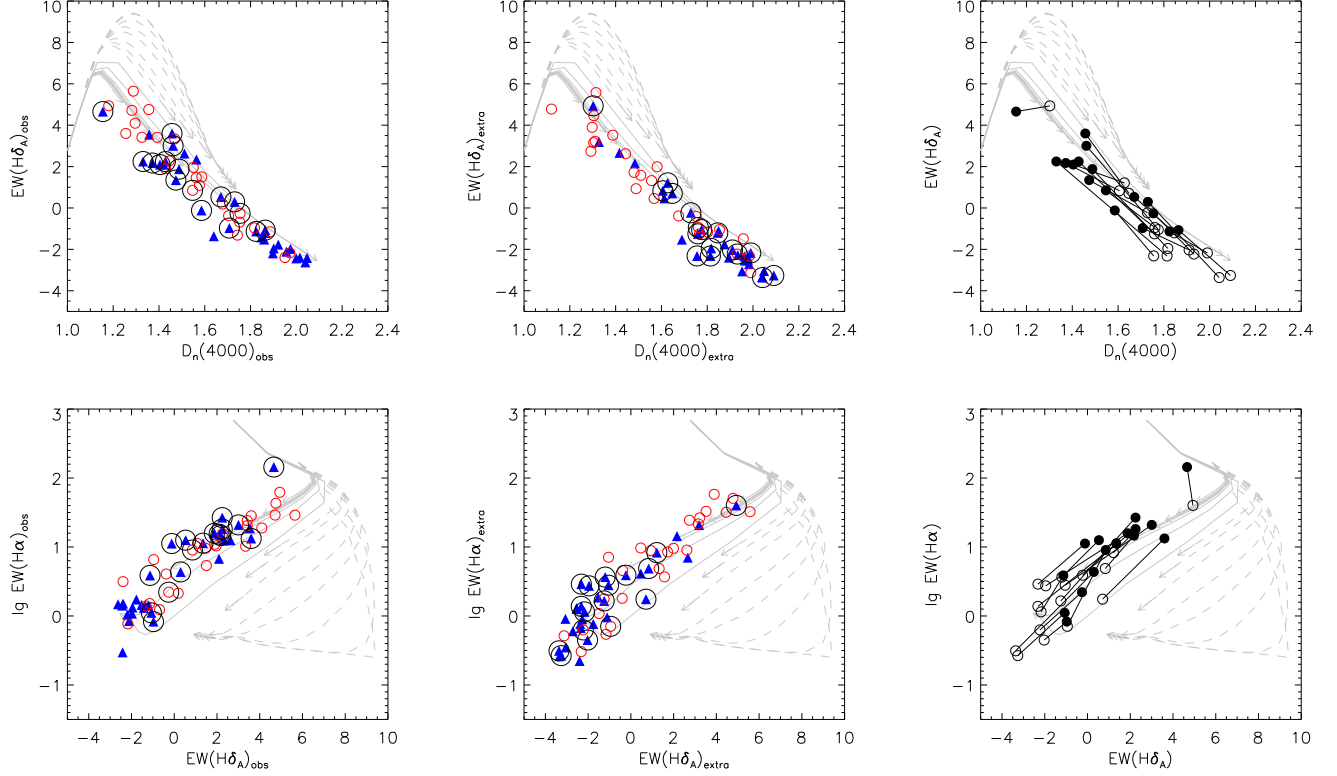


FIG. 9.— Our galaxies are plotted as colorful symbols on planes of  $D_n(4000)$  vs.  $EW(H\delta_A)$  (upper panels) and  $EW(H\delta_A)$  vs.  $EW(H\alpha)$  (lower panels). Shown by solid and dashed lines are solar-metallicity models of continuous star formation histories and star formation bursts from the stellar population synthesis code of [Bruzual & Charlot \(2003\)](#). The left panels are based on the observed emission line measurements, and the middle panels based on the inward extrapolation of the radial profiles. The right panel shows the turnover galaxies only, but for both observed (open circles) and inward extrapolated (solid circles) measurements, with the solid lines connecting the two measurements of each galaxy.

$D_n(4000)$  slope shows good correlations with both the observed and the extrapolated  $D_n(4000)$ , in the sense that galaxies with a larger  $D_n(4000)$  in their center present steeper (more negative) slope, namely, having smaller  $D_n(4000)$  in the outskirts compared to the central region. The  $D_n(4000)$  slope increases from around zero at the smallest central  $D_n(4000)$  ( $\sim 1.2$ ) to  $\sim -0.8$  at the largest central  $D_n(4000)$  ( $\sim 2$ ). This correlation is consistent with the *inside-out* picture of the star formation quenching in galaxies, in which the star formation gets shut down firstly in the galactic center, before extending to larger and larger radii.

Different to the unbarred galaxies, the barred galaxies as a whole show no clear correlations in either case. It is interesting that, however, they behave quite differently when divided into two subsets, with and without turnover feature. The barred galaxies without turnover feature are mostly located in the region with high- $D_n(4000)$  and flat slope, well deviating from the area of the unbarred galaxies. The large central  $D_n(4000)$  and the flat slope combine to suggest that both the center and the outer region of these galaxies are dominated by old stellar populations. In contrast, the turnover galaxies follow a tight correlation between the observed central  $D_n(4000)$  and the slope, which is similar to, but even tighter than the unbarred galaxies. When plotted with the extrapolated  $D_n(4000)$  the turnover galaxies move towards area of larger  $D_n(4000)$ , located in between the

unbarred galaxies and the non-turnover barred galaxies. The different behaviors of the different types of galaxies are more clearly shown in the right-most panel of the same figure where the  $D_n(4000)$  slope is plotted against the observed-to-extrapolated  $D_n(4000)$  difference.

As a complementary analysis, the lower panel of Figure 10 shows the gradient of luminosity-weighted stellar age as a function of the observed (left) and extrapolated (middle) central age, and the difference between the two. The stellar age of given spaxel in the datacubes is estimated using the **STARLIGHT** code as described in §2. The age gradient is given by the slope of the linear fit to the inner region of the age profile, over the same radial range adopted to fit the  $D_n(4000)$  profile. The central extrapolated age is obtained by extrapolating the fitted profile towards the galactic center, in the same ways as in case of  $D_n(4000)$ . The behaviors of the central ages and age gradient are in good agreement with what are shown in the upper panels. We have also estimated mass-weighted ages, finding much smaller gradients and weaker turnover features when compared to those from the luminosity-weighted ages. This can be understood from the fact that young stellar populations contribute a large fraction of the total luminosity but the stellar mass is more dominated by old populations. Therefore, the flatter profile of the mass-weighted profiles and the lack of central turnover suggest that, it is the young populations formed in the recent past that dominate both the

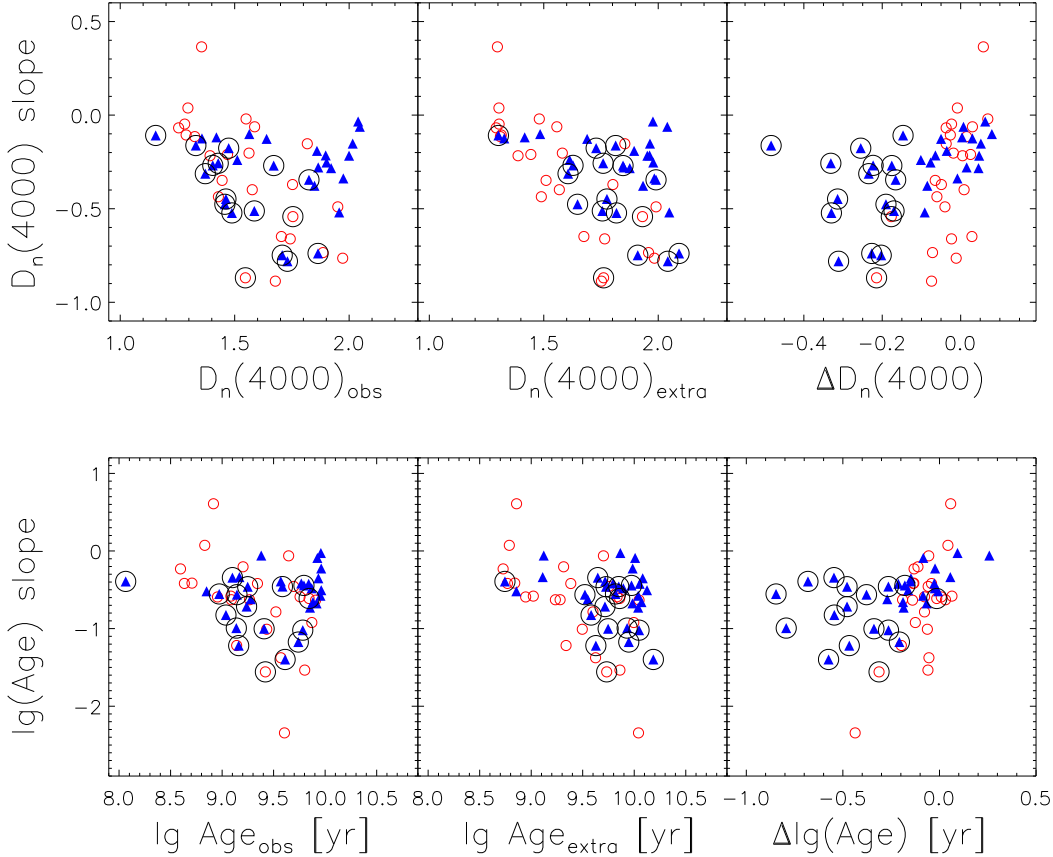


FIG. 10.— *Upper*: slope of the inner profile of  $D_n(4000)$  as a function of the observed central  $D_n(4000)$  (left), the inward extrapolation of the central  $D_n(4000)$  (middle), and the difference between the observed and extrapolated central  $D_n(4000)$  (right). *Lower*: Luminosity-weighted stellar population age gradients as a function of the observed central ages (left), extrapolated central ages (middle) and  $\Delta \text{Age}$  values (right). Symbols and colors are the same as in Figure 4.

central turnover feature and the overall stellar population gradient.

#### 4. DISCUSSION

##### 4.1. Is the turnover always present simultaneously in the three parameters?

In this work we have defined our turnover galaxies according to their  $D_n(4000)$  profile only. We note that, 5 of the 57 galaxies in our sample present significant central upturn in  $\text{EW}(\text{H}\delta_A)$  or  $\text{EW}(\text{H}\alpha)$ , but they show no turnover feature in  $D_n(4000)$ . We divide them into two subsets and discuss their properties separately in the following two paragraphs.

The first subset consists of 4 galaxies: *IC 1256*, *NGC 3106*, *UGC 11649* and *UGC 12224*. These galaxies present a central upturn in  $\text{EW}(\text{H}\alpha)$ , with no significant turnover feature in  $D_n(4000)$  or  $\text{EW}(\text{H}\delta_A)$ . This subset includes both barred and unbarred galaxies (see Table 1), with their center being classified as either star-forming region or LINER on the BPT diagram. *NGC 3106* shows ring-like tidal tails in the outskirts, with a close faint companion galaxy in the SDSS image. *UGC 11649* is a barred galaxy, with an outer ring-like structure. *IC 1256* is an unbarred spiral with an inner ring, with surrounding faint galaxies shown in the SDSS image. We note that this galaxy also show turnover in  $\text{EW}(\text{H}\delta_A)$ , though not in

$D_n(4000)$ . *UGC 12224* is a Sc type galaxy with very diffuse spiral arms. The upturn of  $\text{EW}(\text{H}\alpha)$  indicates the enhancement of central star formation in these galaxies, which might be triggered by tidal interactions (e.g. *NGC 3106*, *IC 1256*) or other mechanisms. The central star formation enhancement must have started very recently, considering the lack of similar turnover feature in  $D_n(4000)$  and  $\text{EW}(\text{H}\delta_A)$  which indicate stellar populations formed in the past.

The other subset has only one galaxy, *NGC 7563*, which shows turnover only in  $\text{EW}(\text{H}\delta_A)$ . This is a barred, early-type (Sa) spiral. It has a faint ring-like structure in the outskirts, with no obvious spiral arms. Color-mass diagram suggests this is a passive red galaxy. The  $D_n(4000)$  is above 1.6 across the galaxy, and the  $\text{H}\alpha$  emission is very weak everywhere. The enhanced  $\text{EW}(\text{H}\delta_A)$  in the center implies the existence of massive young stars, and thus rejuvenate recent star formation. The origin of this star formation, however, is unclear based on our data alone.

Having discussed these exceptional cases where  $D_n(4000)$  turnover is not associated with the turnover in  $\text{EW}(\text{H}\delta_A)$  or  $\text{EW}(\text{H}\alpha)$ , now we come back to the galaxies with  $D_n(4000)$  turnover. As mentioned earlier (§3.2), most of the galaxies with turnover in  $D_n(4000)$  also present turnover feature in  $\text{EW}(\text{H}\delta_A)$  and/or  $\text{EW}(\text{H}\alpha)$ . Indeed, this is the case for 12 out of 15 galaxies that we



identify to have a central turnover in  $D_n(4000)$ .

The rest three galaxies are *NGC 0036*, *NGC 3381* and *NGC 4210*. They show turnover feature in  $D_n(4000)$ , but not in the other two parameters. We find that, the  $D_n(4000)$  turnover in *NGC 0036* and *NGC 4210* are actually very weak; the profiles of all the three parameters are close to be flat, with slight decrease in  $D_n(4000)$  and weak upturn in  $EW(H\delta_A)$  and  $EW(H\alpha)$  towards the smallest radii. In Figure 4, the two galaxies are very close to the  $1 - \sigma$  line which separates the turnover and non-turnover classes. The third galaxy, *NGC 3381*, similarly shows a weak turnover feature in both  $D_n(4000)$  and  $EW(H\alpha)$ , but there is no obvious turnover in  $EW(H\delta_A)$ . Therefore, for these galaxies, the central behaviors of the three parameters are not necessarily inconsistent with each other, and their different turnover classes should not be emphasized. We should be safe to claim that, most (if not all) of the galaxies with a  $D_n(4000)$  turnover also present turnover feature in both  $EW(H\delta_A)$  and  $EW(H\alpha)$ .

This finding is striking given the known fact that the three diagnostic parameters are sensitive to different ages of stellar populations. The fact that the central enhancement in both  $EW(H\delta_A)$  and  $EW(H\alpha)$  are always associated with the central decrease of  $D_n(4000)$  implies that, no matter what physical processes are responsible for the turnover feature, they must have been at work continuously since at least 1-2 Gyr ago, and are still working at the present day. It is natural to conjecture that the several galaxies with central turnover only in  $EW(H\alpha)$  but no feature in other parameters are at the early stage of this long term event, expected to present turnover feature in  $EW(H\delta_A)$  and  $D_n(4000)$  at later times. We would like to point that, however, in order to better understand these exceptional galaxies, one would need larger samples that allow better statistics.

#### 4.2. *Is the presence of a bar a necessary condition for the turnover feature?*

The most striking result produced by the current work is that, almost all the turnover galaxies in our sample host a bar structure, whereas only half of the barred galaxies present turnover feature. This result appears to suggest that the presence of a bar is a necessary, but not sufficient condition for the central turnover to occur.

The three diagnostic parameters are known to be sensitive indicators of different ages of stellar populations. Therefore, for a given spaxel in the datacubes, these parameters combine to roughly tell the recent star formation history of the corresponding region within the galaxy. The “turnover” of these diagnostic parameters thus reveals recent/ongoing star formation occurring in the galactic center over the past 1-2 Gyr, which makes the central region younger than one would expect for a galaxy of the same kind. Our work thus provides direct evidence for the bar-induced star formation enhancement in the central region of galaxies.

The contrast in nuclear star formation between barred and unbarred galaxies was first observed more than forty years ago based on radio continuum surveys (Cameron 1971; Dressel & Condon 1978; Dressel 1979; Heckman 1980; Hummel 1980, 1981). By contrasting the global radio luminosity with the nuclear radio luminosity for both barred and unbarred galaxies, these early studies detected a marked excess of nuclear star formation in

$\sim 30 - 50\%$  of barred systems (see reviews by Kennicutt (1994, 1998); Kormendy & Kennicutt (2004)). In a recent work, Wang et al. (2012) analyzed a sample of  $\sim 1500$  barred galaxies identified from SDSS, finding the central star formation rate (as inferred by  $H\alpha$  luminosity measured from the SDSS 3''-fiber spectroscopy) to be enhanced in strongly barred galaxies. These authors also found that not all the barred galaxies showed central enhanced star formation rates. Our results are in good agreement with these previous studies. With the help of both the resolved spectroscopy from the CALIFA IFU and the high resolution optical image from SDSS, we are allowed to probe the radial gradient of the recent star formation history for different structural components separately.

However, Wang et al. (2012) found that only 50% of the galaxies with central SFR enhancement host a strong bar. In contrast, we find almost all the turnover galaxies are barred. This discrepancy may be attributed to the different sample selections adopted in the two studies. Although both works select relatively face-on late-type galaxies, one important difference is that our sample excludes merging/interacting systems. As those authors suggested, the central SFR enhancement in the unbarred galaxies may be caused by other processes such as galaxy-galaxy interactions. In consistent with this suggestion, a study of a complete sample of  $\sim 10^5$  star-forming galaxies in SDSS revealed that only  $\sim 40\%$  of the most strongly star-forming systems have companion galaxies within  $\sim 70$  kpc. Therefore, based on both Li et al. (2008) and Wang et al. (2012), it is likely that both the internal bar structure and tidal interactions with other galaxies are responsible for the central star formation enhancement as observed in a complete sample of nearby galaxies. It'd be interesting to extend the IFU-based analysis presented in this paper to samples of merging galaxies, galaxies with close companions and those located in crowded regions. This will be our next step, in which we will make use of the ongoing MaNGA survey which provides much larger sample covering wider ranges in galaxy mass, color, morphology and environment.

#### 4.3. *Implications for bar-driven gas inflow as origin of the central turnover feature*

Both theoretical studies and  $N$ -body simulations have well established that bars in galaxies grow through transferring angular momentum to the outer disk, which drives the gas outward (if located outside corotation) to form an outer ring, or inward (if inside corotation) to fall to the center (see Sellwood & Wilkinson 1993, for a review). This gas infall is believed to make pseudobulges through the induced star formation in the central region (see Kormendy & Kennicutt 2004, and references therein). Our results agree well with this picture. The color-mass diagram in Figure 5 shows that the turnover galaxies are mostly bluer than  $NUV-r \sim 4 - 5$ , bluer than those non-turnover barred galaxies. Since  $NUV-r$  is a sensitive indicator of the cold gas content of galaxies (Zhang et al. 2009; Li et al. 2012), our result suggests the turnover galaxies contain more cold gas than those non-turnover galaxies. This supports the bar-driven gas inflow as the driving process for the central star formation and the resulting turnover feature, as observed in some of the barred galaxies. This might be one of the

reasons for the absence of turnover feature in half of our barred galaxies which have redder NUV- $r$  color and thus don't have substantially high fraction of cold gas in their disk.

The intermittent nature of bar-induced gas inflow might be another reason why the turnover is not always seen in barred galaxies. Simulations show that the inflowing gas will first be accumulated at the ends of the bar, before it can further fall inward through loss of angular momentum (Combes 2007). The inflow timescale is very short ( $\sim 10$  Myr) compared with the typical lifetime of bars (Combes 2007). Similar hints come from studies of star-forming nuclear rings which are also related to the bar-driven gas transport from disk to galactic center. Sarzi et al. (2007) found that circumnuclear star formation is most likely to experience episodic starbursts rather than constant star formation. High star formation rates in the central part of the galaxy can exhaust the gas very quickly, turning off the star formation, which will restart until more gas is supplied inside. However, our  $D_n(4000)$ -EW( $H\delta_A$ ) and EW( $H\delta_A$ )-EW( $H\alpha$ ) diagrams show that the central star formation history in the turnover galaxies closely follows models of continuous star formation, and this is true for both the observed and the extrapolated values of the diagnostic parameters (see Figure 9).

Based on CALIFA/DR1 data, Holmes et al. (2015) have attempted to search for bar-like bisymmetric non-circular flow, believed to be a signature of gas inflow. We note that 6 of our turnover galaxies were included in that work, of which 3 showed non-circular flows (NGC 0477, UGC 03253 and NGC 7321) and 1 presented warped flow (NGC 0036). The warped flow may be not driven by bars, but rather results from an oval disk which drives gas infall in a similar way to what a bar does (Kormendy & Kennicutt 2004, and references therein). Considering the short time scale of gas infall and the relatively longer period of the induced star formation, perhaps it is not surprising to see no non-circular flow in some of our turnover galaxies.

In addition to bar-driven instabilities and tidal interactions discussed above, other mechanisms have been suggested to pull more gas inward from outer disks, such as spiral-driven instabilities (Sellwood 2011) and angular momentum exchange with the hosting dark matter halo (Athanasoula 2003). In any case, a common purpose of all these mechanisms is to bring the cold gas in disk to the central region. In order for a complete picture of the driving processes for the gas inflow, one would need to observationally map the molecular gas distribution from outer disks down to small galactic centric radii with spatial resolution comparable to the current IFU instruments.

#### 4.4. Implications for growth/rejuvenation of pseudobulges

Our finding of the recent/ongoing star formation as inferred from the central turnover of the diagnostic parameters provides strong support to theoretical expectations that bar-driven gas flow triggers star formation activity in the central region, which leads to ongoing growth of the central (pseudo) bulge. In fact, the role of bars in building up pseudobulges in galactic centers, and consequently driving the secular evolu-

tion of galaxies, has a rich history of research over more than four decades, and obtained great attention particularly in the past decade or so (see the comprehensive reviews by Kormendy 1993; Sellwood & Wilkinson 1993; Kormendy & Kennicutt 2004; Sellwood 2014; Kormendy 2013). As reviewed by Kormendy & Kennicutt (2004), many barred galaxies (and oval galaxies) have very active star formation in their bulge. In a recent work, Coelho & Gadotti (2011) applied stellar population synthesis to a sample of 575 galaxy bulges in the SDSS, finding the barred galaxies with  $\lg(M_*/M_\odot) \gtrsim 10$  to show a bimodal distribution of bulge ages: a normal distribution with mean age of 10.7 Gyr which is comparable to unbarred galaxies of similar stellar masses, and an excessive young population with mean age of 4.7 Gyr which is not seen in unbarred galaxies. The authors suggested that the excess of young population in the bulges was an evidence for the rejuvenation of bulges as induced by bar-driven star formation. Simulation analysis by Spinoso et al. (2016) also shown evidence that bar has the impact on the evolution of the gas and stellar components of the galaxy in the central region.

Our result is consistent with Coelho & Gadotti (2011) in the sense that we also find both young populations (and ongoing star formation) and old populations in the bulge-region of our galaxies. This can be seen from the lower-left panel of Figure 10: the barred galaxies with no central turnover are located in the large-age and flat-slope region, and the barred galaxies with turnover feature are located in the region of younger ages and steeper slopes, forming an anti-correlation of age versus slope. When plotted using the inward extrapolation of the linear fit to the observed profile at larger radii, the turnover galaxies move significantly toward regions of older ages and flatter slopes, thus close to (thought not exactly the same as) the non-turnover barred galaxies. This implies that, the bulge which has stopped star formation long ago and is dominated by very old populations ( $\sim 10$  Gyr) becomes actively forming stars and younger, due to the ongoing/recent star formation induced by bar-driven gas inflow. A direct comparison with Coelho & Gadotti (2011) is not applicable, and for this one needs to perform stellar population synthesis to the IFU spectra in order to decompose the young population contributed by the bar-driven star formation from the underlying old population. This can well be a topic for future IFU-based studies.

## 5. CONCLUSIONS

For a sample of 57 nearly face-on spiral galaxies selected from the CALIFA/DR2 sample, we have performed photometric decomposition of their bulge/bar/disk components using optical image from SDSS, and obtained two-dimensional maps and radial profiles of  $D_n(4000)$ , EW( $H\delta_A$ ) and EW( $H\alpha$ ) using the integral field spectroscopy from CALIFA. We identify a class of "turnover" galaxies whose inner-most region shows significant drop in  $D_n(4000)$ , and/or corresponding upturn in EW( $H\delta_A$ ) and EW( $H\alpha$ ). We investigate the recent star formation history, as indicated by the three diagnostic parameters, for the central region of the both turnover and non-turnover galaxies, and we compare the results for barred and unbarred populations, as well as for galaxies with different global properties.

Our conclusions can be summarized as follows.

1. We find strong link between the central turnover feature with the bar structure in galaxies. Out of the 57 galaxies in our sample, 17 are identified as a turnover galaxy, of which 15 are barred. On the other hand, however, only half of the barred galaxies present the central turnover, indicating that the presence of a bar is a necessary, but not sufficient condition for the turnover feature to occur, at least for the sample being studied.
2. The majority of the turnover galaxies identified by the central turnover in  $D_n(4000)$  also present corresponding turnover feature in the profiles of  $EW(H\alpha)$  and  $EW(H\delta_A)$ . Both the observed values of these diagnostic parameters and the values from inward extrapolation of the linear fits to the profiles at larger radii are consistent with models in which star formation declines continuously, suggesting that the central region of these galaxies have been forming stars continuously in the past 1-2 Gyr.
3. The turnover galaxies are found to have intermediate NUV- $r$  colors ( $3 < \text{NUV-}r < 5$ ), while their centers are mostly classified as star-forming regions according to both the central  $D_n(4000)$  and the BPT diagram. When using the measurements from inward extrapolation of radial profiles at larger radii, these galaxies move largely towards the quiescent sequence with  $D_n(4000) > 1.6$  and the AGN or AGN/SF composite regions.
4. In addition to the presence of the bar structure, the size of the bar (normalized by the disk radius) is the only galaxy property that is found to correlate with the turnover feature: the longer the bar, the larger the turnover region. There is no correlation of turnover size with galaxy stellar mass, NUV- $r$  color, or the axial ratio of the bar.
5. Our results provide strong support to the expectations that bar-driven gas inflow triggers star formation in galaxy centers, which makes/grows/rejuvenates pseudobulges.

Our work demonstrates the power of integral field spectroscopy for studying the resolved star formation history of galaxies. The complementary photometric decomposition is also helpful and even necessary in this work. A lesson we have learned is that, one may easily misidentify the turnover feature due to incorrect radial range adopted for the linear fitting. The bulge/bar radii obtained from the photometric decomposition have allowed us to take data well within the inner region, avoiding contamination from the spiral disk.

We would like to point out that, however, the current work is limited by the small sample size of the CALIFA survey. The exclusion of merging systems from our sample is another thing one should keep in mind. A more complete sample covering wide ranges of galaxy mass, morphology and environment is needed in order for a full understanding of the central turnover. Such data is becoming available thanks to the SDSS-IV/MaNGA survey (Bundy et al. 2015). We plan to extend our analysis to a much larger sample based on the MaNGA data, including galaxies with masses down to  $10^9 M_\odot$  and those in merging/interacting systems, and examining the connections with both the internal structural properties such as the bar and external environment.

We thank the anonymous referee for his or her careful and helpful comments, which improved the quality of the paper immensely. This work is supported by National Key Basic Research Program of China (No. 2015CB857004), NSFC (Grant No. 11173045, 11233005, 11325314, 11320101002) and the Strategic Priority Research Program “The Emergence of Cosmological Structures” of CAS (Grant No. XDB09000000). Data used in this study comes from the Calar Alto Legacy Integral Field Area (CALIFA) survey (<http://califa.caha.es/>) and the Sloan Digital Sky Survey (SDSS). Based on observations collected at the Centro Astronómico Hispano Alemán (CAHA) at Calar Alto, operated jointly by the Max-Planck-Institut für Astronomie and the Instituto de Astrofísica de Andalucía (CSIC).

Funding for the SDSS and SDSS-II has been provided by the Alfred P. Sloan Foundation, the Participating Institutions, the National Science Foundation, the U.S. Department of Energy, the National Aeronautics and Space Administration, the Japanese Monbukagakusho, the Max Planck Society, and the Higher Education Funding Council for England. The SDSS Web Site is <http://www.sdss.org/>. The SDSS is managed by the Astrophysical Research Consortium for the Participating Institutions. The Participating Institutions are the American Museum of Natural History, Astrophysical Institute Potsdam, University of Basel, University of Cambridge, Case Western Reserve University, University of Chicago, Drexel University, Fermilab, the Institute for Advanced Study, the Japan Participation Group, Johns Hopkins University, the Joint Institute for Nuclear Astrophysics, the Kavli Institute for Particle Astrophysics and Cosmology, the Korean Scientist Group, the Chinese Academy of Sciences (LAMOST), Los Alamos National Laboratory, the Max-Planck-Institute for Astronomy (MPIA), the Max-Planck-Institute for Astrophysics (MPA), New Mexico State University, Ohio State University, University of Pittsburgh, University of Portsmouth, Princeton University, the United States Naval Observatory, and the University of Washington.

## REFERENCES

- Athanassoula, E. 1992, MNRAS, 259, 345  
Athanassoula, E. 2003, MNRAS, 341, 1179  
Baldwin, J. A., Phillips, M. M., & Terlevich, R. 1981, PASP, 93, 5  
Balogh, M. L., Morris, S. L., Yee, H. K. C., Carlberg, R. G., & Ellingson, E. 1999, ApJ, 527, 54  
Barazza, F. D., Jablonka, P., Desai, V., et al. 2009, A&A, 497, 713  
Barazza, F. D., Jogee, S., & Marinova, I. 2008, ApJ, 675, 1194  
Blanton, M. R., Eisenstein, D., Hogg, D. W., Schlegel, D. J., & Brinkmann, J. 2005, ApJ, 629, 143  
Blanton, M. R., Kazin, E., Muna, D., Weaver, B. A., & Price-Whelan, A. 2011, AJ, 142, 31  
Blanton, M. R., & Roweis, S. 2007, AJ, 133, 734  
Blanton, M. R., Schlegel, D. J., Strauss, M. A., et al. 2005, AJ, 129, 2562



- Bruzual, G., & Charlot, S. 2003, MNRAS, 344, 1000
- Bundy, K., Bershad, M. A., Law, D. R., et al. 2015, ApJ, 798, 7
- Cacho, R., Sánchez-Blázquez, P., Gorgas, J., & Pérez, I. 2014, MNRAS, 442, 2496
- Cameron, M. J. 1971, MNRAS, 152, 439
- Cardelli, J. A., Clayton, G. C., & Mathis, J. S. 1989, ApJ, 345, 245
- Carollo, C. M., Scarlata, C., Stiavelli, M., Wyse, R. F. G., & Mayer, L. 2007, ApJ, 658, 960
- Cheung, E., Trump, J. R., Athanassoula, E., et al. 2015, MNRAS, 447, 506
- Cid Fernandes, R., González Delgado, R. M., García Benito, R., et al. 2014, A&A, 561, A130
- Cid Fernandes, R., Gu, Q., Melnick, J., et al. 2004, MNRAS, 355, 273
- Cid Fernandes, R., Pérez, E., García Benito, R., et al. 2013, A&A, 557, A86
- Coelho, P., & Gadotti, D. A. 2011, ApJ, 743, L13
- Combes, F. 2007, IAU Symposium, 235, 19
- Comerón, S., Knapen, J. H., & Beckman, J. E. 2008, A&A, 485, 695
- de Jong, T., Clegg, P. E., Rowan-Robinson, M., et al. 1984, ApJ, 278, L67
- de Vaucouleurs, G. 1963, ApJS, 8, 31
- Devereux, N. 1987, ApJ, 323, 91
- Dressel, L. L. 1979, Ph.D. Thesis,
- Dressel, L. L., & Condon, J. J. 1978, ApJS, 36, 53
- Ellison, S. L., Nair, P., Patton, D. R., et al. 2011, MNRAS, 416, 2182
- Emsellem, E., Greusard, D., Combes, F., et al. 2001, A&A, 368, 52
- Erwin, P., Saglia, R. P., Fabricius, M., et al. 2015, MNRAS, 446, 4039
- Eskridge, P. B., Frogel, J. A., Pogge, R. W., et al. 2000, AJ, 119, 536
- Gadotti, D. A., Seidel, M. K., Sánchez-Blázquez, P., et al. 2015, A&A, 584, A90
- García-Benito, R., Zibetti, S., Sánchez, S. F., et al. 2015, A&A, 576, A135
- Girardi, L., Bressan, A., Bertelli, G., & Chiosi, C. 2000, A&AS, 141, 371
- Hawarden, T. G., Mountain, C. M., Leggett, S. K., & Puxley, P. J. 1986, MNRAS, 221, 41P
- He, Y. Q., Xia, X. Y., Hao, C. N., et al. 2013, ApJ, 773, 37
- Heckman, T. M. 1980, A&A, 87, 152
- Ho, L. C., Filippenko, A. V., & Sargent, W. L. W. 1997, ApJ, 487, 591
- Holmes, L., Spekkens, K., Sánchez, S. F., et al. 2015, MNRAS, 451, 4397
- Hummel, E. 1981, A&A, 93, 93
- Hummel, E. 1980, A&AS, 41, 151
- Hummer, D. G., & Storey, P. J. 1987, MNRAS, 224, 801
- Hunter, D. A., & Elmegreen, B. G. 2004, AJ, 128, 2170
- Husemann, B., Jahnke, K., Sánchez, S. F., et al. 2013, A&A, 549, A87
- Jogee, S., Scoville, N., & Kenney, J. D. P. 2005, ApJ, 630, 837
- Kannappan, S. J., Jansen, R. A., & Barton, E. J. 2004, AJ, 127, 1371
- Kauffmann, G., Heckman, T. M., White, S. D. M., et al. 2003, MNRAS, 341, 33
- Kennicutt, R. C., Jr. 1998, ARA&A, 36, 189
- Kennicutt, R. C., Jr. 1994, Mass-Transfer Induced Activity in Galaxies, 131
- Knapen, J. H., Shlosman, I., & Peletier, R. F. 2000, ApJ, 529, 93
- Kormendy, J. 1993, Galactic Bulges, 153, 209
- Kormendy, J. 2013, Secular Evolution of Galaxies, 1
- Kormendy, J., Drory, N., Bender, R., & Cornell, M. E. 2010, ApJ, 723, 54
- Kormendy, J., & Kennicutt, R. C., Jr. 2004, ARA&A, 42, 603
- Lee, G.-H., Park, C., Lee, M. G., & Choi, Y.-Y. 2012, ApJ, 745, 125
- Lee, G.-H., Woo, J.-H., Lee, M. G., et al. 2012, ApJ, 750, 141
- Li, C., Gadotti, D. A., Mao, S., & Kauffmann, G. 2009, MNRAS, 397, 726
- Li, C., Kauffmann, G., Fu, J., et al. 2012, MNRAS, 424, 1471
- Li, C., Kauffmann, G., Heckman, T. M., Jing, Y. P., & White, S. D. M. 2008, MNRAS, 385, 1903
- Li, C., Wang, E., Lin, L., et al. 2015, ApJ, 804, 125
- Lin, Y., Cervantes Sodi, B., Li, C., Wang, L., & Wang, E. 2014, ApJ, 796, 98
- Makarov D., Prugniel P., Terekhova N., Courtois H., & Vauglin I. 2014, A&A, 570, A13
- Masters, K. L., Nichol, R. C., Hoyle, B., et al. 2011, MNRAS, 411, 2026
- Méndez-Abreu, J., Debattista, V. P., Corsini, E. M., & Aguerri, J. A. L. 2014, A&A, 572, A25
- Marinova, I., & Jogee, S. 2007, ApJ, 659, 1176
- Martin, P., & Roy, J.-R. 1994, ApJ, 424, 599
- Martin, D. C., Fanson, J., Schiminovich, D., et al. 2005, ApJ, 619, L1
- Obreja, A., Domínguez-Tenreiro, R., Brook, C., et al. 2013, ApJ, 763, 26
- Pérez, I., Sánchez-Blázquez, P., & Zurita, A. 2009, A&A, 495, 775
- Peng, C. Y., Ho, L. C., Impey, C. D., & Rix, H.-W. 2002, AJ, 124, 266
- Puxley, P. J., Hawarden, T. G., & Mountain, C. M. 1988, MNRAS, 234, 29P
- Piner, B. G., Stone, J. M., & Teuben, P. J. 1995, ApJ, 449, 508
- Regan, M. W., & Teuben, P. J. 2004, ApJ, 600, 595
- Regan, M. W., Thornley, M. D., Vogel, S. N., et al. 2006, ApJ, 652, 1112
- Sánchez, S. F., García-Benito, R., Zibetti, S., et al. 2016, arXiv:1604.02289
- Sánchez, S. F., Kennicutt, R. C., Gil de Paz, A., et al. 2012, A&A, 538, AA8
- Sánchez, S. F., Rosales-Ortega, F. F., Iglesias-Páramo, J., et al. 2014, A&A, 563, A49
- Sánchez-Blázquez, P., Ocvirk, P., Gibson, B. K., Pérez, I., & Peletier, R. F. 2011, MNRAS, 415, 709
- Sánchez-Blázquez, P., Rosales-Ortega, F. F., Méndez-Abreu, J., et al. 2014, A&A, 570, A6
- Sánchez-Menguiano, L., Sánchez, S. F., Pérez, I., et al. 2016, A&A, 587, A70
- Sakamoto, K., Okumura, S. K., Ishizuki, S., & Scoville, N. Z. 1999, ApJ, 525, 691
- Sarzi, M., Allard, E. L., Knapen, J. H., & Mazzuca, L. M. 2007, MNRAS, 380, 949
- Sellwood, J. A. 2014, Reviews of Modern Physics, 86, 1
- Sellwood, J. A. 2011, MNRAS, 410, 1637
- Sellwood, J. A., & Wilkinson, A. 1993, Reports on Progress in Physics, 56, 173
- Sheth, K., Vogel, S. N., Regan, M. W., et al. 2002, AJ, 124, 2581
- Sheth, K., Vogel, S. N., Regan, M. W., Thornley, M. D., & Teuben, P. J. 2005, ApJ, 632, 217
- Sheth, K., Elmegreen, D. M., Elmegreen, B. G., et al. 2008, ApJ, 675, 1141-1155
- Skrutskie, M. F., Cutri, R. M., Stiening, R., et al. 2006, AJ, 131, 1163
- Spinoso, D., Bonoli, S., Dotti, M., et al. 2016, arXiv:1607.02141
- Thomas, D., & Davies, R. L. 2006, MNRAS, 366, 510
- Walcher, C. J., Wisotzki, L., Bekeraité, S., et al. 2014, A&A, 569, AA1
- Wang, J., Kauffmann, G., Overzier, R., et al. 2012, MNRAS, 423, 3486
- Worthey, G., & Ottaviani, D. L. 1997, ApJS, 111, 377
- York, D. G., Adelman, J., Anderson, J. E., Jr., et al. 2000, AJ, 120, 1579
- Zhang, W., Li, C., Kauffmann, G., et al. 2009, MNRAS, 397, 1243
- Zaritsky, D., Kennicutt, R. C., Jr., & Huchra, J. P. 1994, ApJ, 420, 87
- Zurita, A., & Pérez, I. 2008, A&A, 485, 5
- Zhou, Z.-M., Cao, C., & Wu, H. 2015, AJ, 149, 1



TABLE 1  
THE PHOTOMETRIC PARAMETERS OF BULGE, BAR AND DISK.

Galaxy 1	Hubble Type 2	Bar Type <sup>a</sup> 3	Bar Type <sup>b</sup> 4	$\mu_e$ (mag arcsec <sup>-2</sup> ) 5	$r_e$ (arcsec) 6	$n$ 7	$\mu_0$ (mag arcsec <sup>-2</sup> ) 8	$h$ (arcsec) 9	$\mu_{e,bar}$ (mag arcsec <sup>-2</sup> ) 10	$r_{e,bar}$ (arcsec) 11	
UGC00005	Sbc	A	A	22.80±0.09	1.26±0.01	0.61±0.28	21.74±0.18	7.83±1.00	...	...	
NGC7819	Sc	A	A	21.78±0.02	2.04±0.04	0.79±0.09	22.95±0.01	12.43±0.03	...	...	
UGC00036	Sab	AB	A	20.85±0.00	1.16±0.03	1.05±0.15	21.04±0.02	5.36±0.09	...	...	
NGC0001	Sbc	A	A	20.04±0.00	1.30±0.01	0.68±0.16	20.87±0.01	5.89±0.02	...	...	
NGC0036	Sb	B	B	20.50±0.01	0.71±0.02	0.63±0.01	21.78±0.01	9.87±0.07	21.94±0.01	2.40±0.01	0.6
NGC0171	Sb	B	B	21.16±0.01	1.55±0.01	0.68±0.01	21.84±0.01	13.96±0.05	22.31±0.01	4.08±0.00	0.4
NGC0180	Sb	B	B	21.61±0.00	1.30±0.00	0.66±0.02	22.50±0.01	17.48±0.08	22.48±0.00	3.34±0.00	0.8
NGC0237	Sc	B	A	21.30±0.01	0.32±0.01	0.17±0.05	20.78±0.00	6.25±0.03	...	...	
NGC0477	Sbc	AB	B	22.45±0.01	1.19±0.00	0.88±0.10	22.50±0.01	11.65±0.86	22.79±0.01	2.15±0.01	0.3
IC1683	Sb	AB	A	20.40±0.01	1.10±0.03	0.62±0.27	21.56±0.01	6.61±0.13	...	...	
NGC0496	Scd	A	A	22.77±0.02	1.11±0.02	0.72±0.19	22.30±0.05	9.77±1.47	...	...	
NGC0776	Sb	B	B	21.66±0.00	1.66±0.02	0.41±0.01	21.89±0.01	10.63±0.12	21.40±0.06	1.92±0.07	1.1
UGC03253	Sb	B	B	21.20±0.00	0.93±0.00	0.62±0.02	21.81±0.01	8.47±0.38	22.35±0.02	2.10±0.00	0.4
NGC2253	Sbc	B	B	21.43±0.02	0.97±0.02	0.17±0.03	21.07±0.01	8.57±0.07	20.54±0.01	0.96±0.00	1.2
NGC2347	Sbc	AB	A	20.77±0.00	1.26±0.00	0.86±0.00	20.52±0.00	6.65±0.00	...	...	
NGC2449	Sab	AB	B	23.06±0.01	1.12±0.01	0.17±0.12	21.12±0.03	7.04±0.06	21.22±0.00	1.57±0.00	0.7
NGC2730	Scd	B	B	23.31±0.01	1.07±0.01	0.43±0.07	22.81±0.01	14.28±0.26	23.65±0.00	2.83±0.00	0.7
NGC2906	Sbc	A	A	20.61±0.00	1.41±0.00	0.85±0.01	20.96±0.00	9.17±0.03	...	...	
NGC2916	Sbc	A	A	20.17±0.02	1.06±0.04	0.51±0.03	21.16±0.01	8.77±0.02	...	...	
UGC05108	Sb	B	B	21.09±0.01	0.81±0.01	0.63±0.02	21.26±0.01	4.99±0.03	22.43±0.01	1.39±0.01	0.1
NGC3106	Sab	A	A	20.90±0.01	2.51±0.02	1.72±0.03	22.36±0.12	14.39±0.31	...	...	
NGC3381	Sd	B	B	21.82±0.01	1.04±0.02	1.05±0.12	22.22±0.02	14.25±0.36	22.59±0.01	2.88±0.01	0.3
IC0674	Sab	B	B	20.62±0.02	1.01±0.01	0.65±0.01	21.43±0.01	6.01±0.04	22.24±0.01	2.26±0.02	0.2
NGC3614	Sbc	AB	A	23.17±0.01	3.35±0.01	1.12±0.12	22.60±0.02	21.68±0.10	...	...	
NGC3811	Sbc	B	B	25.96±0.02	3.41±0.04	1.42±0.01	21.84±0.04	12.84±0.23	20.53±0.02	1.80±0.10	1.1
UGC07012	Scd	AB	A	23.27±0.00	3.91±0.01	1.02±0.03	22.50±0.03	8.55±0.16	...	...	
NGC4185	Sbc	AB	A	22.27±0.01	2.14±0.01	0.83±0.12	22.22±0.02	16.25±0.10	...	...	
NGC4210	Sb	B	B	21.82±0.02	0.93±0.01	0.60±0.11	21.77±0.01	12.90±0.05	21.87±0.01	2.04±0.00	0.4
NGC4470	Sc	A	A	23.86±0.00	1.07±0.01	0.84±0.02	21.25±0.01	20.08±0.06	...	...	
NGC5000	Sbc	B	B	21.31±0.01	0.80±0.01	0.51±0.05	22.61±0.00	11.37±0.05	23.42±0.00	4.46±0.00	1.1
NGC5205	Sbc	B	A	21.60±0.00	2.17±0.01	0.83±0.53	21.77±0.01	10.77±0.08	...	...	
UGC08781	Sb	B	B	20.48±0.02	0.96±0.01	0.99±0.07	21.98±0.01	8.80±0.05	22.03±0.01	2.43±0.00	0.6
NGC5378	Sb	B	B	20.51±0.07	1.30±0.14	1.01±0.08	22.47±0.00	15.83±0.06	22.65±0.04	4.42±0.06	0.5
NGC5406	Sb	B	B	20.29±0.00	1.13±0.00	0.51±0.01	21.54±0.01	13.16±0.05	21.85±0.01	2.92±0.00	1.1
NGC5520	Sbc	A	A	20.29±0.01	1.44±0.02	0.53±0.04	20.88±0.01	6.92±0.01	...	...	
NGC5720	Sbc	B	B	20.95±0.02	1.16±0.02	0.77±0.12	22.36±0.01	10.09±0.06	22.52±0.01	2.50±0.01	0.4
UGC09476	Sbc	A	A	22.45±0.01	1.54±0.01	0.69±0.12	22.17±0.02	11.23±0.10	...	...	
NGC5888	Sb	B	B	21.62±0.01	1.41±0.01	0.71±0.02	21.48±0.00	10.35±0.04	23.39±0.01	3.20±0.01	0.9
IC4566	Sb	B	B	21.24±0.02	1.86±0.01	0.91±0.11	22.11±0.01	12.08±0.04	23.49±0.01	2.20±0.01	0.1
NGC6004	Sbc	B	B	20.72±0.09	0.93±0.19	0.64±0.10	22.12±0.01	14.03±0.19	22.99±0.04	2.45±0.05	0.5
NGC6063	Sbc	A	A	22.99±0.07	1.20±0.21	0.78±0.04	22.28±0.00	11.38±0.06	...	...	
NGC6154	Sab	B	B	26.99±0.01	3.95±0.02	0.17±0.11	22.23±0.01	11.76±0.03	21.49±0.01	2.24±0.02	1.4
IC1256	Sb	AB	B	21.86±0.01	0.91±0.01	0.80±0.02	22.16±0.02	9.12±0.03	27.08±0.00	5.39±0.01	0.1
NGC6497	Sab	B	B	20.36±0.01	1.07±0.01	1.03±0.02	21.51±0.01	7.67±0.04	22.40±0.00	2.62±0.03	0.3
NGC6941	Sb	B	B	20.81±0.01	1.39±0.03	0.78±0.04	22.49±0.01	19.48±0.03	22.50±0.01	4.38±0.00	0.4
UGC11649	Sab	B	B	21.97±0.02	1.71±0.03	1.02±0.07	22.54±0.01	12.37±0.05	22.83±0.01	3.78±0.00	0.4
NGC7321	Sbc	B	B	21.33±0.01	0.83±0.02	0.47±0.07	21.50±0.01	11.14±0.12	22.21±0.01	3.03±0.02	1.0
UGC12224	Sc	A	A	23.29±0.00	1.80±0.00	1.05±0.18	23.03±0.01	16.19±0.04	...	...	
NGC7466	Sbc	A	A	20.97±0.02	1.59±0.01	0.75±0.01	22.14±0.00	12.35±0.05	...	...	
NGC7489	Sbc	A	A	22.43±0.01	1.08±0.01	0.71±0.03	22.24±0.00	9.94±0.06	...	...	
NGC7549	Sbc	B	B	23.51±0.02	1.45±0.00	0.86±0.08	21.69±0.00	8.41±0.04	23.01±0.62	2.30±0.83	0.6
NGC7563	Sa	B	B	19.95±0.00	1.01±0.00	0.89±0.05	21.92±0.01	10.71±0.02	21.14±0.00	3.66±0.00	0.7
NGC7591	Sbc	B	B	20.49±0.01	0.33±0.01	0.36±0.08	20.72±0.01	6.02±0.02	21.41±0.11	0.34±0.36	0.1
NGC7653	Sb	A	A	20.87±0.01	1.95±0.01	1.17±0.32	21.61±0.07	9.57±0.08	...	...	
NGC7716	Sb	A	A	20.11±0.01	2.17±0.01	1.15±0.12	21.72±0.02	13.02±0.10	...	...	
UGC12816	Sc	A	A	23.22±0.01	2.53±0.01	1.04±0.58	22.65±0.07	8.93±0.13	...	...	
NGC5947	Sbc	B	B	21.03±0.02	0.73±0.01	0.42±0.11	22.04±0.01	9.35±0.04	21.53±0.01	1.94±0.01	1.0

<sup>a</sup>Bar classification by CALIFA team (Walcher et al. 2014): ‘A’ for unbarred, ‘B’ for barred, ‘AB’ if unsure.

<sup>b</sup>Our bar classification used in this work: ‘A’ for unbarred, ‘B’ for barred.

TABLE 2  
THE CENTRAL OBSERVED AND EXTRAPOLATED VALUES AND THE GRADIENTS.

Galaxy	$D_n(4000)$			SSP-AGE			$R_t('')$
	$Cen_{obs}$	$Cen_{extra}$	Slope(dex/ $R_e$ )	$Cen_{obs}$	$Cen_{extra}$	Slope(dex/ $R_e$ )	
UGC00005	$1.58 \pm 0.09$	$1.57 \pm 0.10$	$-0.40 \pm 0.30$	$9.43 \pm 0.15$	$9.50 \pm 0.28$	$-1.01 \pm 0.87$	...
NGC7819	$1.18 \pm 0.01$	$1.12 \pm 0.11$	$0.64 \pm 0.42$	$8.24 \pm 0.05$	$8.31 \pm 0.33$	$1.33 \pm 1.21$	...
UGC00036	$1.82 \pm 0.12$	$1.85 \pm 0.22$	$-0.15 \pm 0.42$	$9.65 \pm 0.05$	$9.70 \pm 0.21$	$-0.06 \pm 0.37$	...
NGC0001	$1.56 \pm 0.02$	$1.58 \pm 0.10$	$-0.20 \pm 0.15$	$9.34 \pm 0.02$	$9.38 \pm 0.25$	$-0.42 \pm 0.41$	...
NGC0036	$1.86 \pm 0.05$	$2.09 \pm 0.28$	$-0.74 \pm 0.72$	$9.78 \pm 0.02$	$10.05 \pm 0.41$	$-1.02 \pm 1.09$	3.00
NGC0171	$1.85 \pm 0.19$	$1.93 \pm 0.29$	$-0.38 \pm 0.87$	$9.85 \pm 0.25$	$10.04 \pm 0.36$	$-0.73 \pm 1.03$	...
NGC0180	$1.33 \pm 0.08$	$1.81 \pm 0.62$	$-0.16 \pm 1.79$	$8.97 \pm 0.23$	$9.82 \pm 0.49$	$-0.55 \pm 1.38$	5.00
NGC0237	$1.47 \pm 0.03$	$1.44 \pm 0.18$	$-0.21 \pm 0.46$	$9.27 \pm 0.03$	$9.23 \pm 0.61$	$-0.63 \pm 1.56$	...
NGC0477	$1.40 \pm 0.03$	$1.63 \pm 0.26$	$-0.27 \pm 0.68$	$9.14 \pm 0.05$	$9.52 \pm 0.42$	$-0.56 \pm 1.12$	4.00
IC1683	$1.36 \pm 0.03$	$1.30 \pm 0.24$	$0.36 \pm 0.51$	$8.92 \pm 0.04$	$8.86 \pm 0.59$	$0.61 \pm 1.21$	...
NGC0496	$1.26 \pm 0.03$	$1.29 \pm 0.09$	$-0.07 \pm 0.33$	$8.60 \pm 0.08$	$8.73 \pm 0.30$	$-0.23 \pm 1.21$	...
NGC0776	$1.49 \pm 0.03$	$1.82 \pm 0.42$	$-0.52 \pm 0.98$	$9.24 \pm 0.03$	$9.72 \pm 0.73$	$-0.72 \pm 1.78$	5.00
UGC03253	$1.47 \pm 0.06$	$1.73 \pm 0.17$	$-0.18 \pm 0.38$	$9.25 \pm 0.12$	$9.73 \pm 0.27$	$-0.46 \pm 0.61$	3.00
NGC2253	$1.37 \pm 0.02$	$1.61 \pm 0.08$	$-0.31 \pm 0.25$	$9.04 \pm 0.05$	$9.58 \pm 0.20$	$-0.83 \pm 0.64$	3.00
NGC2347	$1.70 \pm 0.04$	$1.68 \pm 0.19$	$-0.65 \pm 0.47$	$9.57 \pm 0.06$	$9.62 \pm 0.40$	$-1.38 \pm 1.05$	...
NGC2449	$1.86 \pm 0.05$	$1.85 \pm 0.34$	$-0.28 \pm 0.72$	$9.77 \pm 0.03$	$9.80 \pm 0.57$	$-0.42 \pm 1.21$	...
NGC2730	$1.36 \pm 0.02$	$1.33 \pm 0.13$	$-0.12 \pm 0.49$	$8.85 \pm 0.10$	$8.86 \pm 0.62$	$-0.52 \pm 2.37$	...
NGC2906	$1.89 \pm 0.00$	$1.96 \pm 0.09$	$-0.73 \pm 0.37$	$9.76 \pm 0.01$	$9.83 \pm 0.16$	$-0.59 \pm 0.57$	...
NGC2916	$1.75 \pm 0.08$	$1.93 \pm 0.28$	$-0.54 \pm 0.76$	$9.84 \pm 0.09$	$9.86 \pm 0.26$	$-0.61 \pm 0.75$	3.00
UGC05108	$1.67 \pm 0.07$	$1.85 \pm 0.22$	$-0.27 \pm 0.34$	$9.59 \pm 0.08$	$9.85 \pm 0.26$	$-0.46 \pm 0.45$	3.00
NGC3106	$1.95 \pm 0.03$	$1.99 \pm 0.24$	$-0.49 \pm 0.85$	$9.91 \pm 0.02$	$10.05 \pm 0.43$	$-0.63 \pm 1.44$	...
NGC3381	$1.15 \pm 0.05$	$1.30 \pm 0.09$	$-0.11 \pm 0.31$	$8.06 \pm 0.29$	$8.74 \pm 0.39$	$-0.39 \pm 1.36$	3.00
IC0674	$2.00 \pm 0.01$	$1.95 \pm 0.15$	$-0.22 \pm 0.23$	$9.96 \pm 0.02$	$10.12 \pm 0.15$	$-0.51 \pm 0.26$	...
NGC3614	$1.55 \pm 0.02$	$1.76 \pm 0.27$	$-0.87 \pm 1.04$	$9.42 \pm 0.06$	$9.73 \pm 0.51$	$-1.56 \pm 2.11$	4.00
NGC3811	$1.46 \pm 0.07$	$1.78 \pm 0.27$	$-0.45 \pm 0.59$	$9.14 \pm 0.07$	$9.93 \pm 0.38$	$-0.99 \pm 0.90$	5.00
UGC07012	$1.29 \pm 0.05$	$1.31 \pm 0.09$	$-0.11 \pm 0.23$	$8.63 \pm 0.19$	$8.77 \pm 0.35$	$-0.42 \pm 0.94$	...
NGC4185	$1.74 \pm 0.00$	$1.77 \pm 0.08$	$-0.66 \pm 0.41$	$9.80 \pm 0.03$	$9.86 \pm 0.20$	$-1.53 \pm 0.96$	...
NGC4210	$1.71 \pm 0.09$	$1.91 \pm 0.12$	$-0.75 \pm 0.45$	$9.74 \pm 0.14$	$9.95 \pm 0.23$	$-1.17 \pm 0.81$	3.00
NGC4470	$1.28 \pm 0.02$	$1.30 \pm 0.07$	$-0.05 \pm 0.21$	$8.71 \pm 0.07$	$8.84 \pm 0.26$	$-0.41 \pm 0.79$	...
NGC5000	$1.43 \pm 0.02$	$1.76 \pm 0.27$	$-0.26 \pm 0.49$	$9.10 \pm 0.02$	$9.65 \pm 0.39$	$-0.34 \pm 0.72$	3.00
NGC5205	$1.75 \pm 0.04$	$1.80 \pm 0.11$	$-0.37 \pm 0.27$	$9.69 \pm 0.05$	$9.75 \pm 0.26$	$-0.46 \pm 0.69$	...
UGC08781	$1.90 \pm 0.18$	$1.96 \pm 0.11$	$-0.22 \pm 0.20$	$9.84 \pm 0.09$	$10.05 \pm 0.18$	$-0.42 \pm 0.33$	...
NGC5378	$1.90 \pm 0.03$	$1.98 \pm 0.47$	$-0.25 \pm 0.97$	$9.96 \pm 0.02$	$9.87 \pm 0.72$	$-0.03 \pm 1.44$	...
NGC5406	$1.97 \pm 0.02$	$1.98 \pm 0.19$	$-0.34 \pm 0.61$	$9.87 \pm 0.04$	$9.89 \pm 0.17$	$-0.48 \pm 0.53$	...
NGC5520	$1.39 \pm 0.11$	$1.39 \pm 0.21$	$-0.22 \pm 0.47$	$9.09 \pm 0.29$	$9.02 \pm 0.85$	$-0.58 \pm 1.96$	...
NGC5720	$1.96 \pm 0.07$	$2.05 \pm 0.14$	$-0.52 \pm 0.36$	$9.95 \pm 0.02$	$10.04 \pm 0.13$	$-0.58 \pm 0.38$	...
UGC09476	$1.43 \pm 0.03$	$1.49 \pm 0.10$	$-0.44 \pm 0.39$	$9.14 \pm 0.05$	$9.34 \pm 0.34$	$-1.22 \pm 1.47$	...
NGC5888	$2.02 \pm 0.03$	$1.96 \pm 0.14$	$-0.15 \pm 0.31$	$9.96 \pm 0.01$	$9.98 \pm 0.15$	$-0.23 \pm 0.32$	...
IC4566	$1.92 \pm 0.07$	$1.88 \pm 0.17$	$-0.28 \pm 0.47$	$9.92 \pm 0.07$	$9.98 \pm 0.29$	$-0.68 \pm 0.72$	...
NGC6004	$1.46 \pm 0.02$	$1.65 \pm 0.10$	$-0.48 \pm 0.42$	$9.16 \pm 0.04$	$9.63 \pm 0.22$	$-1.22 \pm 0.87$	3.00
NGC6063	$1.59 \pm 0.02$	$1.56 \pm 0.09$	$-0.06 \pm 0.32$	$9.52 \pm 0.05$	$9.60 \pm 0.31$	$-0.78 \pm 1.01$	...
NGC6154	$2.04 \pm 0.07$	$1.98 \pm 0.23$	$-0.03 \pm 0.47$	$9.93 \pm 0.02$	$10.08 \pm 0.26$	$-0.35 \pm 0.53$	...
IC1256	$1.51 \pm 0.02$	$1.61 \pm 0.08$	$-0.24 \pm 0.15$	$9.28 \pm 0.03$	$9.55 \pm 0.20$	$-0.62 \pm 0.36$	...
NGC6497	$1.64 \pm 0.02$	$1.69 \pm 0.11$	$-0.13 \pm 0.23$	$9.57 \pm 0.05$	$9.72 \pm 0.39$	$-0.39 \pm 0.77$	...
NGC6941	$1.82 \pm 0.09$	$1.99 \pm 0.28$	$-0.35 \pm 0.84$	$9.79 \pm 0.11$	$9.97 \pm 0.23$	$-0.44 \pm 0.70$	3.00
UGC11649	$1.86 \pm 0.04$	$1.89 \pm 0.30$	$-0.19 \pm 0.64$	$9.88 \pm 0.04$	$10.07 \pm 0.34$	$-0.66 \pm 0.72$	...
NGC7321	$1.73 \pm 0.05$	$2.04 \pm 0.16$	$-0.78 \pm 0.29$	$9.61 \pm 0.05$	$10.19 \pm 0.32$	$-1.40 \pm 0.56$	4.00
UGC12224	$1.45 \pm 0.04$	$1.51 \pm 0.14$	$-0.35 \pm 0.69$	$9.09 \pm 0.07$	$9.28 \pm 0.29$	$-0.63 \pm 1.45$	...
NGC7466	$1.55 \pm 0.01$	$1.48 \pm 0.23$	$-0.02 \pm 0.49$	$9.20 \pm 0.09$	$9.31 \pm 0.42$	$-0.20 \pm 0.91$	...
NGC7489	$1.30 \pm 0.00$	$1.30 \pm 0.17$	$0.04 \pm 0.58$	$8.83 \pm 0.01$	$8.79 \pm 0.37$	$0.07 \pm 1.21$	...
NGC7549	$1.42 \pm 0.05$	$1.42 \pm 0.22$	$-0.12 \pm 0.44$	$9.17 \pm 0.10$	$9.11 \pm 0.62$	$-0.34 \pm 1.18$	...
NGC7563	$2.05 \pm 0.03$	$2.04 \pm 0.48$	$-0.06 \pm 0.41$	$9.92 \pm 0.02$	$10.01 \pm 0.43$	$-0.09 \pm 0.36$	...
NGC7591	$1.56 \pm 0.02$	$1.48 \pm 0.28$	$-0.10 \pm 0.67$	$9.38 \pm 0.06$	$9.12 \pm 0.59$	$-0.06 \pm 1.30$	...
NGC7653	$1.68 \pm 0.07$	$1.75 \pm 0.30$	$-0.89 \pm 0.72$	$9.61 \pm 0.13$	$10.04 \pm 0.59$	$-2.34 \pm 1.52$	...
NGC7716	$1.97 \pm 0.02$	$1.98 \pm 0.27$	$-0.76 \pm 0.79$	$9.87 \pm 0.02$	$10.00 \pm 0.26$	$-0.92 \pm 0.78$	...
UGC12816	$1.33 \pm 0.01$	$1.31 \pm 0.05$	$-0.11 \pm 0.17$	$8.96 \pm 0.05$	$8.95 \pm 0.29$	$-0.59 \pm 0.87$	...
NGC5947	$1.59 \pm 0.02$	$1.76 \pm 0.06$	$-0.51 \pm 0.17$	$9.41 \pm 0.02$	$9.75 \pm 0.16$	$-1.00 \pm 0.43$	3.00

TABLE 3  
STATISTICS OF TURNOVERS FROM DIFFERENT PROFILES.

	Total	$N_t$		
		$D_n(4000)$	$EW(H\delta)^a$	$EW(H\alpha)^b$
All galaxies	57	17	15(14)	22(15)
Bar	32	15	13(12)	16(13)
unBar	25	2	2(2)	6(2)

NOTE. —

<sup>a</sup>The number in brackets means the number of galaxies reveal turnover in both  $EW(H\delta)$  and  $D_n(4000)$  profiles.

<sup>b</sup>The number in brackets means the number of galaxies reveal turnover in both  $EW(H\alpha)$  and  $D_n(4000)$  profiles.